Composite Structures 178 (2017) 63–86

Contents lists available at ScienceDirect

Composite Structures

journal homepage: www.elsevier.com/locate/compstruct

Static analysis of stepped functionally graded magneto-electro-elastic plates in thermal environment: A finite element study

M. Vinyas, S.C. Kattimani *

Department of Mechanical Engineering, National Institute of Technology Karnataka, Surathkal 575025, India

ARTICLE INFO

Article history:
Received 29 March 2017
Revised 5 June 2017
Accepted 29 June 2017
Available online 1 July 2017

Keywords:
Magneto-electro-elastic
Pyroeffects
Temperature distributions
Functionally graded materials

ABSTRACT

In this article, a finite element (FE) formulation accounting for multiphysics response of multilayered magneto-electro-elastic (MEE) plates in the thermal environment has been presented. The equilibrium equations of motion are attained using the principle of total potential energy and coupled constitutive relations of MEE material. Maxwell's equation of electrostatics and magnetostatics are used to model the electric and magnetic behavior. The influence of various through thickness temperature distributions on the static parameters of stepped functionally graded magneto-electro-elastic (*SFG*-MEE) plates is investigated. Further, an extra attention has been devoted to evaluate the effect of product properties (pyroelectric and pyromagnetic coupling), boundary conditions and aspect ratio on the direct (displacements, electric potential and magnetic potential) and derived quantities (stresses, electric displacement, and magnetic flux density) of the *SFG*-MEE plate. A comparative study is also carried out to analyse the effect of stacking sequence, boundary conditions, pyroeffects, length-to-width ratio and aspect ratios of the *SFG*-MEE plate. The credibility of the proposed FE model is verified with the results available in the literature. It is expected that the findings in this article may be useful for accurate design and analysis of MEE structures under the thermal environment.

1. Introduction

Recently, intelligent structures have drawn a significant attention of the researchers in various engineering fields. These sophisticated and multifunctional structures exploit the exceptional characteristics of smart materials. Among them, the magneto-electro-elastic (MEE) material is a prominent smart material which displays unique energy conversion capabilities between magnetic, electric and elastic fields. In addition, they also exhibit different cross properties which include magneto-electro-elastic, magneto-elastic and electro-elastic field interactions which are absent in individual constituents. This makes them adaptable to various potential applications such as actuators, sensors, transducers, stability control etc. It is found that the intelligent structures made of functionally graded (FG) materials display a better structural performance than the conventional composite materials particularly, in the thermal environment. More recently, FG materials are used to make effective utilization of MEE coupling properties. Hence, much of the investigations are being carried out on the FG-MEE structures (plates, beams, and shells). Many researchers performed the free vibration analysis of MEE structures adopting various computational techniques such as exact solution method [1–3], discrete layer approximate method [4–7], state vector method [8–11], finite element method [12–14] etc. Using an asymptotic approach Tsai et al. [15] presented a three-dimensional (3D) free vibration analysis of doubly curved FG-MEE shells with open-circuit surface conditions. Ebrahimi and Barati [16] analysed the free vibration characteristics of smart nanostructures through a nonlocal higher-order refined magneto-electro-viscoelastic beam model. In addition, Shooshtari and Razavi [17] evaluated the free vibration characteristics of MEE rectangular plate with the aid of higher order shear deformation theory. Nonlinear vibration control of MEE plates and shells using active constrained layer damping treatment has been studied by Kattimani and Ray [18,19] considering different stacking sequence and boundary conditions. They extended their analysis to the functionally graded MEE plates also [20]. The smart damping of nonlinear vibrations of FG plates in the thermal environment using piezoelectric composites was investigated by Panda and Ray [21]. Later, Sarangi and Ray [22] extended the similar analysis to doubly curved FG shells in the thermal environment. The peculiar multiphysics coupled response of MEE structures has motivated many researchers to investigate its static behavior under various loading

* Corresponding author.
E-mail address: sck@nitk.ac.in (S.C. Kattimani).

http://dx.doi.org/10.1016/j.compstruct.2017.06.068
0263-8223/

conditions [23–28]. Additionally, Zheng et al. [29] investigated the nonlinear static behavior of MEE plates by employing transverse shear deformation theory and von Karman plate theory. Pan and Waksmanski [30] presented an exact closed form solution for three-dimensional deformation of a layered MEE plate with non-local effect. Sladek et al. [31–33] evaluated the bending analysis of MEE plates using a meshless approach based on the local Petrov – Galerkin approach. Wang and Pan [34] developed a 3D FE formulation to evaluate the bending response of FG multiferroic composites under different loading conditions. Considering imperfect interfacial bonding, Nazargah and Cheragi [35] presented a 3D formulation to analyse the bending behavior of FG-MEE plates resting on elastic foundation. The stability analysis of MEE structures under various loading conditions was also investigated [36–38]. In accordance with the non-local theory and Timoshenko beam theory, Ebrahimi and Barati [39] analysed the buckling behavior of functionally graded MEE nanoplates resting on Winkler- Pasternak foundation through refined plate theory. Meanwhile, in the application of sensors and actuators, an optimal design of MEE structures becomes prominent. Loja et al. [40] performed the optimization studies to minimize the deformed profile shape of FG-MEE beam using differential evolution technique. In order to achieve maximum conversion efficiency from mechanical energy to electric and magnetic energy, Sun and Kim [41] formulated a systematic design optimization method for the optimal layering of MEE composites. The optimization of the effective magnetoelectric voltage coefficient of fibrous composites made of piezoelectric and piezomagnetic phases was carried out by Kuo and Wang [42].

Due to predominant use of MEE structures in sensors and actuators, a clear understanding of such structures exposed to thermal environment is very much essential. Some of the scholars have tried to fill the gaps in the analysis of MEE structures subjected to thermal loading. Sunar [43] derived the constitutive equations for the thermopiezomagnetic continuum with the aid of FE formulation. Badri and Kayiem [44] investigated the static and dynamic analysis of magneto-thermo-electro-elastic (MTEE) plates. An exact solution was developed by Ootao and Tanigawa [45] to analyse the transient behavior of multilayered magneto-thermo-electro-elastic (MTEE) strip subjected to non-uniform and unsteady heating. Kumaravel et al. [46] studied the influence of both uniform and non-uniform load on the static behavior of MEE beam. An additional coupling between thermo-electric and thermo-magnetic fields result in the development of pyroloads which affects the behavior of MEE structures significantly. Kondaiah et al. [47–49] considered the effect of pyroelectric and pyromagnetic coupling to investigate the static behavior of MEE beams and plates. Akbarzadeh and Chen [50] derived analytical solutions and compared the coupled response of functionally graded and homogeneous thermo-magneto-electro-elastic hollow cylinder. Meanwhile, Ebrahimi and Barati [51] studied the influence of different temperature loads on the free vibration behavior of FG-MEE nanobeams. In case of stepped functionally graded magneto-electro-elastic (*SFG*-MEE) structure, each layer possesses different thermal expansion coefficient. This leads to a unique variation of displacements, electric potential, magnetic potential and stresses under thermal loading. To this end, it is prominent to study the influence of through thickness temperature distribution on the structural behavior of *SFG*-MEE structures.

This investigation makes the first attempt to evaluate the influence of various through thickness temperature distributions on the direct (displacements, electric potential and magnetic potential) and derived quantities (stresses, electric displacement, and magnetic flux density) of the *SFG*-MEE plate. A FE formulation for multilayered MEE plate has been derived using the principle of total potential energy and coupled constitutive equations of MEE material. The equilibrium equations are solved using condensation method. Few numerical examples are solved to understand the influence of stacking sequence, boundary conditions, length-to-width ratio and aspect ratio on the static behavior of MEE plate. Finally, a special emphasize has been placed on analyzing the contribution of pyroeffects which drastically affects the coupled response of *SFG*-MEE plate. It can be said that the various temperature profiles considered in the present analysis closely resemble the heat sources used in real time application. Hence, it is believed that the proposed FE formulation may be useful to achieve the accurate design and analysis of MEE structures in the different thermal environment.

2. Formulation of the problem

2.1. Geometry and coordinate system

A schematic representation of stepped functionally graded magneto-electro-elastic (*SFG*-MEE) plate occupying the domain $a \times b \times h$ with respect to a Cartesian coordinate system (*x, y, z*) is depicted in Fig. 1. The various boundary conditions considered for the analysis are illustrated in Fig. 2(a)–(e), respectively. The constraints corresponding to the different boundary conditions are given as follows:

$$\text{Clamped edge (C)}: \quad u_x = u_y = u_z = \phi = \psi = 0 \tag{1.a}$$

$$\text{Free edge (F)} \quad : u_x = u_y = u_z = \phi = \psi \neq 0 \tag{1.b}$$

$$\text{Simply supported edge (S)}: \quad u_x \neq 0;\ u_y = u_z = \phi = \psi = 0 \text{ at } x = 0, a$$

$$u_y \neq 0;\ u_x = u_z = \phi = \psi = 0 \text{ at } y = 0, b \tag{1.c}$$

2.2. Constitutive equations

The coupled constitutive equations of MEE material considering thermal fields, as adaptable in the present finite element formulation can be expressed as follows:

$$\{\sigma^n\} = [C^n]\{\varepsilon^n\} - [e^n]\{E^n\} - [q^n]\{H^n\} - \{\lambda^n\} \tag{2.a}$$

$$\{D^n\} = [e^n]^T\{\varepsilon^n\} + [\eta^n]\{E^n\} + [m^n]\{H^n\} + \{p^n\}\Delta\theta \tag{2.b}$$

$$\{B^n\} = [q^n]^T\{\varepsilon^n\} + [m^n]\{E^n\} + [\mu^n]\{H^n\} + \{\tau^n\}\Delta\theta \tag{2.c}$$

$$\{\lambda^n\} = [C^n]\{\alpha^n\}\Delta\theta \tag{2.d}$$

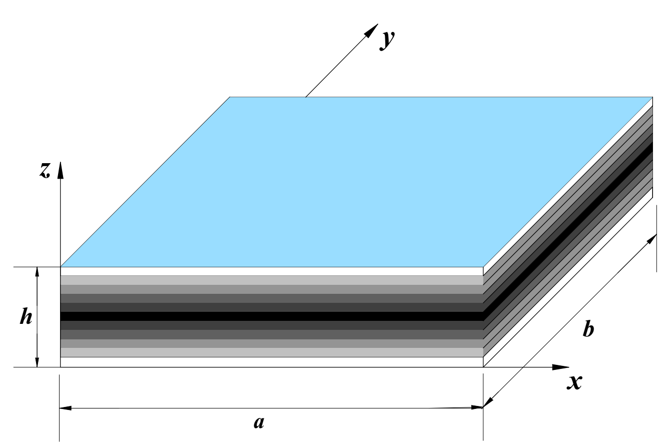

Fig. 1. Schematic representation of *SFG*-MEE plate.

in which, the superscript n represents the layer number under consideration. Also, $n = 1,2,3\ldots N$; where N is the total number of layers. Further, $\Delta\theta$ is the temperature rise from the stress-free reference temperature θ_0. The different matrices and vectors in the Eqs. (2.a)–(2.d) are listed in Appendix A.

2.3. Finite element formulation

The finite element (FE) model of the magneto-electro-elastic (MEE) plate is discretized by eight noded brick element with five degrees of freedom at each node. The generalized displacement vector $\{d_t\}$, the electric potential vector $\{\phi\}$ and the magnetic potential vector $\{\psi\}$ can be expressed in terms of the nodal generalized displacement vector $\{d_t^e\}$, the nodal electric potential vector $\{\phi^e\}$ and the nodal magnetic potential vector $\{\psi^e\}$, respectively as follows:

$$\{d_t\} = [N_t]\{d_t^e\}, \{\phi\} = [N_\phi]\{\phi^e\}, \{\psi\} = [N_\psi]\{\psi^e\} \tag{3}$$

in which,

$$\begin{aligned}&\{d_t^e\} = \left[\{d_{t1}\}^T\{d_{t2}\}^T\ldots\{d_{t8}\}^T\right]^T, \{\phi^e\} = [\phi_1\phi_2\ldots\phi_8]^T, \{\psi^e\} = [\psi_1\psi_2\ldots\psi_8]^T\\&[N_t] = [N_{t1}N_{t2}\ldots N_{t8}], N_{ti} = n_iI_t, [N_\phi] = [n_1n_2\ldots n_8], [N_\psi] = [N_\phi]\end{aligned} \tag{4}$$

where n_i is the natural coordinate shape function associated with the i^{th} node of the element; I_t is the identity matrix; $[N_t]$, $[N_\phi]$ and $[N_\psi]$ are (3×24), (1×8) and (1×8) shape function matrices, respectively.

Using Maxwell's fundamental electrostatic and magnetostatic equations, the electric field and magnetic field can be expressed in the following forms

$$\{E\} = -\phi_{,k} \text{ and } \{H\} = -\psi_{,k} \tag{5}$$

where $k = x$, y and z. By using nodal strain-displacement matrices $[B_t]$, $[B_\phi]$ and $[B_\psi]$, the strain vector, electric field vector and magnetic field vector of the system can be represented in terms of the nodal displacement, nodal electric potential and nodal magnetic potential, respectively as follows:

$$\begin{aligned}\{\varepsilon\} &= [L_tN_t]\{d_t^e\} = [B_t]\{d_t^e\}, \{E\} = [L_\phi N_\phi]\{\phi^e\} = [B_\phi]\{\phi^e\}, \{H\}\\&= [L_\psi N_\psi]\{\psi^e\} = [B_\psi]\{\psi^e\}\end{aligned} \tag{6}$$

where L_t, L_ψ and L_ϕ are the differential operators. The various nodal strain displacement relations can be explicitly represented as follows:

$$[B_t] = \begin{bmatrix} \frac{\partial n_1}{\partial x} & 0 & 0 & \frac{\partial n_2}{\partial x} & 0 & 0 & \cdots & \frac{\partial n_8}{\partial x} & 0 & 0\\ 0 & \frac{\partial n_1}{\partial x} & 0 & 0 & \frac{\partial n_2}{\partial x} & 0 & \cdots & 0 & \frac{\partial n_8}{\partial x} & 0\\ 0 & 0 & \frac{\partial n_1}{\partial z} & 0 & 0 & \frac{\partial n_2}{\partial z} & \cdots & 0 & 0 & \frac{\partial n_8}{\partial z}\\ 0 & \frac{\partial n_1}{\partial z} & \frac{\partial n_1}{\partial y} & 0 & \frac{\partial n_2}{\partial z} & \frac{\partial n_2}{\partial y} & \cdots & 0 & \frac{\partial n_8}{\partial z} & \frac{\partial n_8}{\partial y}\\ \frac{\partial n_1}{\partial z} & 0 & \frac{\partial n_1}{\partial x} & \frac{\partial n_2}{\partial z} & 0 & \frac{\partial n_2}{\partial x} & \cdots & \frac{\partial n_8}{\partial z} & 0 & \frac{\partial n_8}{\partial x}\\ \frac{\partial n_1}{\partial y} & \frac{\partial n_1}{\partial x} & 0 & \frac{\partial n_2}{\partial y} & \frac{\partial n_2}{\partial x} & 0 & \cdots & \frac{\partial n_8}{\partial y} & \frac{\partial n_8}{\partial x} & 0 \end{bmatrix},$$

$$[B_\psi] = \begin{bmatrix} \frac{-\partial n_1}{\partial x} & \frac{-\partial n_2}{\partial x} & \cdots & \frac{-\partial n_8}{\partial x}\\ -\frac{\partial n_1}{\partial y} & -\frac{\partial n_2}{\partial y} & \cdots & -\frac{\partial n_8}{\partial y}\\ -\frac{\partial n_1}{\partial z} & -\frac{\partial n_2}{\partial z} & \cdots & -\frac{\partial n_8}{\partial z} \end{bmatrix}, [B_\phi] = [B_\psi] \tag{7}$$

2.4. Equations of motion

The equilibrium equations of motion corresponding to the *SFG-MEE* plate in the thermal environment are arrived using the principle of total potential energy and coupled constitutive equations. The total potential energy is minimized by equating its first variation to zero. It can be explained as follows:

$$\begin{aligned}T_p &= \tfrac{1}{2}\sum_{n=1}^{N}\left[\int_V^n \delta\{\varepsilon^n\}^T\{\sigma^n\}dV^n - \int_{V^n}\delta[E^n]^T\{D^n\}dV^n - \int_{V^n}\delta[H^n]^T\{B^n\}dV^n\right]\\&\quad - \int_{V^n}\delta\{d_t\}^T\{F_{body}\}dV^n - \delta\{d_t\}^T\{F_{conc}\} - \int_A[\delta\{d_t\}^T\{F_{surface}\} + \delta\{\phi\}Q^\phi\\&\quad + \delta\{\psi\}Q^\psi]dA = 0\end{aligned} \tag{8}$$

The volume of the n^{th} layer is represented by V^n. Further, the surface force, the body force and the point force are represented by $\{F_{surface}\}$, $\{F_{body}\}$ and $\{F_{conc}\}$, respectively. Likewise, Q^ϕ and Q^ψ are the surface electric charge density and magnetic charge density, respectively.

Substitution of Eqs. (2) and (6) in Eq. (8) results in

$$\begin{aligned}T_p = &\tfrac{1}{2}\left\{\int_{V^n}\delta\{d_t^e\}^T[B_t]^T\left(\sum_{n=1}^{N}[C^n]\right)[B_t]\{d_t^e\}dV^n\right.\\&\left.-\int_{V^n}\delta\{d_t^e\}^T[B_t]^T\left(\sum_{n=1}^{N}[e^n]\right)[B_\phi]\{\phi^e\}dV^n\right\}\\&-\tfrac{1}{2}\int_{V^n}\delta\{d_t^e\}^T[B_t]^T\left(\sum_{n=1}^{N}[q^n]\right)[B_\psi]\{\psi^e\}dV^n\\&-\tfrac{1}{2}\int_{V^n}\delta\{d_t^e\}^T[B_t]^T\left(\sum_{n=1}^{N}[C^n]\{\alpha_{V_f}^n\}\right)\Delta\theta dV^n\\&-\tfrac{1}{2}\int_{V^n}\delta\{\phi^e\}^T[B_\phi]^T\left(\sum_{n=1}^{N}[e^n]^T\right)[B_t]\{d_t^e\}dV^n\\&-\tfrac{1}{2}\int_{V^n}\delta\{\phi^e\}^T[B_\phi]^T\left(\sum_{n=1}^{N}[\eta^n]\right)[B_\phi]\{\phi^e\}dV^n\\&-\tfrac{1}{2}\int_{V^n}\delta\{\phi^e\}^T[B_\phi]^T\left(\sum_{n=1}^{N}[m^n]\right)[B_\psi]\{\psi^e\}dV^n\\&-\tfrac{1}{2}\int_{V^n}\delta\{\phi^e\}^T\left(\sum_{n=1}^{N}[B_\phi]^T\{p^n\}\Delta\theta\right)dV^n\\&-\tfrac{1}{2}\int_{V^n}\delta\{\psi^e\}^T[B_\psi]^T\left(\sum_{n=1}^{N}[q^n]^T\right)[B_t]\{d_t^e\}dV^n\\&-\tfrac{1}{2}\int_{V^n}\delta\{\psi^e\}^T[B_\psi]^T\left(\sum_{n=1}^{N}[m^n]\right)[B_\phi]\{\phi^e\}dV^n\\&-\tfrac{1}{2}\int_{V^n}\delta\{\psi^e\}^T[B_\psi]^T\left(\sum_{n=1}^{N}[\mu^n]\right)[B_\psi]\{\psi^e\}dV^n\\&-\tfrac{1}{2}\int_V^n\delta\{\psi^e\}^T\left(\sum_{n=1}^{N}[B_\psi]^T\{\tau^n\}\Delta\theta\right)dV^n\\&-\int_A\delta\left(\{d_t^e\}^T[N_t]^T\{F_{surface}\} + \delta\{\phi^e\}[N_\phi]Q^\phi + \delta\{\psi^e\}[N_\psi]Q^\psi\right)dA\\&-\tfrac{1}{2}\sum_{n=1}^{N}\int_V^n\delta\{d_t^e\}^T[N_t]^T\{F_{body}\}dV^n\\&-\delta\{d_t^e\}^T[N_t]^T\{F_{conc}\} = 0\end{aligned} \tag{9}$$

Further, bifurcating the terms based on the coefficients of $\{d_t^e\}^T$, $\{\phi^e\}^T$ and $\{\psi^e\}^T$ and globalizing we obtain the equations of motion as follows:

$$\begin{aligned}&[K_{tt}^g]\{d_t\} + [K_{t\phi}^g]\{\phi\} + [K_{t\psi}^g]\{\psi\} = \{F_m^g\} + \{F_{th}^g\}\\&[K_{t\phi}^g]^T\{d_t\} - [K_{\phi\phi}^g]\{\phi\} - [K_{\phi\psi}^g]\{\psi\} = \{F_\phi^g\} - \{F_{p.e}^g\}\\&[K_{t\psi}^g]^T\{d_t\} - [K_{\phi\psi}^g]^T\{\phi\} - [K_{\psi\psi}^g]\{\psi\} = \{F_\psi^g\} - \{F_{p.m}^g\}\end{aligned} \tag{10}$$

The notations of the different global stiffness matrices and global load vectors are explicitly described in Appendix A. Meanwhile, the stiffness matrices and the force vectors can be expressed as follows:

$$[K_{tt}^g] = [B_t]^T[[C^1]dV^1 + [C^2]dV^2 + \cdots + [C^N]dV^N][B_t]$$

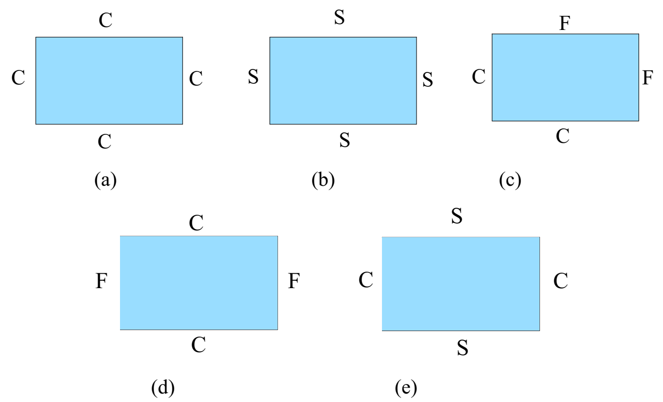

Fig. 2. Boundary conditions (a) clamped on all edges (CCCC) (b) simply supported on all edges (SSSS) (c) adjacent edges clamped (CFFC) (d) opposite edge clamped (FCFC) (e) opposite edges simply supported (CSCS).

$$[K^g_{t\phi}] = [B_t]^T\{[e^1]dV^1 + [e^2]dV^2 + \cdots [e^N]dV^N\}[B_t]$$

$$[K^g_{t\psi}] = [B_t]^T\{[q^1]dV^1 + [q^2]dV^2 + \cdots + [q^N]dV^N\}[B_t]$$

$$[K^g_{\phi\phi}] = [B_\phi]^T\{[\eta^1]dV^1 + [\eta^2]dV^2 + \cdots + [\eta^N]dV^N\}[B_\phi]$$

$$[K^g_{\phi\psi}] = [B_\phi]^T\{[m^1]dV^1 + [m^2]dV^2 + \cdots + [m^N]dV^N\}[B_\phi]$$

$$[K^g_{\psi\psi}] = [B_\psi]^T\{[\mu^1]dV^1 + [\mu^2]dV^2 + \cdots + [\mu^N]dV^N\}[B_\psi]$$

$$\{F^g_m\} = \int_{V^n}[N_t]^T\{F_{body}\}dV^n + \int_A [N_t]^T\{F_{surface}\}dA + [N_t]^T\{F_{conc}\}$$

$$\{F^g_\phi\} = \int_A [N_\phi]^T Q^\phi dA,$$

$$\{F^g_\psi\} = \int_A [N_\psi]^T Q^\psi dA,$$

$$\{F^g_{th}\} = [B_t]\{[C^1]\{\alpha^1\}\Delta\theta^1 dV^1 + [C^2]\{\alpha^2\}\Delta\theta^2 dV^2 + \cdots [C^N]\{\alpha^N\}\Delta\theta^N dV^N\},$$

$$\{F^g_{p.e}\} = [B_\phi]^T\{[p^1]\Delta\theta^1 dV^1 + [p^2]\Delta\theta^2 dV^2 + \cdots + [p^N]\Delta\theta^N dV^N\},$$

$$\{F^g_{p.m}\} = [B_\psi]^T\{[\tau^1]\Delta\theta^1 dV^1 + [\tau^2]\Delta\theta^2 dV^2 + \cdots + [\tau^N]\Delta\theta^N dV^N\} \quad (11)$$

In the present analysis the effect of the mechanical load vector $\{F^g_m\}^T$, the electric load vector $\{F^g_\phi\}^T$ and magnetic load vector $\{F^g_\psi\}^T$ are neglected.

$$[K^g_{tt}]\{d_t\} + [K^g_{t\phi}]\{\phi\} + [K^g_{t\psi}]\{\psi\} = \{F^g_{th}\} \quad (12.a)$$

$$[K^g_{t\phi}]^T\{d_t\} - [K^g_{\phi\phi}]\{\phi\} - [K^g_{\phi\psi}]\{\psi\} = \{F^g_{p.e}\} \quad (12.b)$$

$$[K^g_{t\psi}]^T\{d_t\} - [K^g_{\phi\psi}]^T\{\phi\} - [K^g_{\psi\psi}]\{\psi\} = \{F^g_{p.m}\} \quad (12.c)$$

The displacements due to thermal loads are calculated by condensing the Eqs. 12(a)–(c). The detailed procedure is explicitly described in Appendix B.

Considering the Eq. (12.c) and solving for $\{\psi\}$, we obtain

$$\{\psi\} = [K^g_{\psi\psi}]^{-1}[K^g_{t\psi}]^T\{d_t\} - [K^g_{\psi\psi}]^{-1}[K^g_{\phi\psi}]^T\{\phi\} - [K^g_{\psi\psi}]^{-1}\{F^g_{p.m}\} \quad (13)$$

Similarly, substituting Eq. (13) in Eq. (12.b) and solving for $\{\phi\}$, we get

$$\{\phi\} = [K_2]^{-1}[K_1]\{d_t\} - [K_2]^{-1}\{F_{\phi\_sol}\} \quad (14)$$

Finally, Eqs. (13) and (14) are substituted in Eq. (12.a) to get

$$[K_{eq}]\{d_t\} = \{F_{eq}\} \quad (15)$$

The component stiffness matrices and the equivalent force vectors associated with the Eqs. (14) and (15) are presented in Appendix B.

2.5. Stepped functionally graded (SFG) – MEE plate

Stepped functionally graded stacking sequence of MEE plate is developed by piling up of layers with different volume fraction (V_f) of Barium Titanate ($BaTiO_3$) and Cobalt Ferric Oxide ($CoFe_2O_4$) as demonstrated in Fig. 3(a) and (b). In the case of *SFG-BFB* (*B* labels pure piezoelectric phase and *F* labels pure piezomagnetic phase) MEE plate, the middle layer is composed of pure piezomagnetic phase (V_f = 0.0), while the top and bottom layers are of pure piezoelectric phase (V_f = 1.0). Further, the volume fraction of the intermediate layers varies in steps of 0.2 V_f. Analogously, the piezoelectric phase is replaced by piezomagnetic phase for *SFG-FBF* MEE plate.

2.6. Temperature profiles

The *SFG*-MEE plate is subjected to different temperature profiles which vary across the plate thickness according to the general equations given as follows:

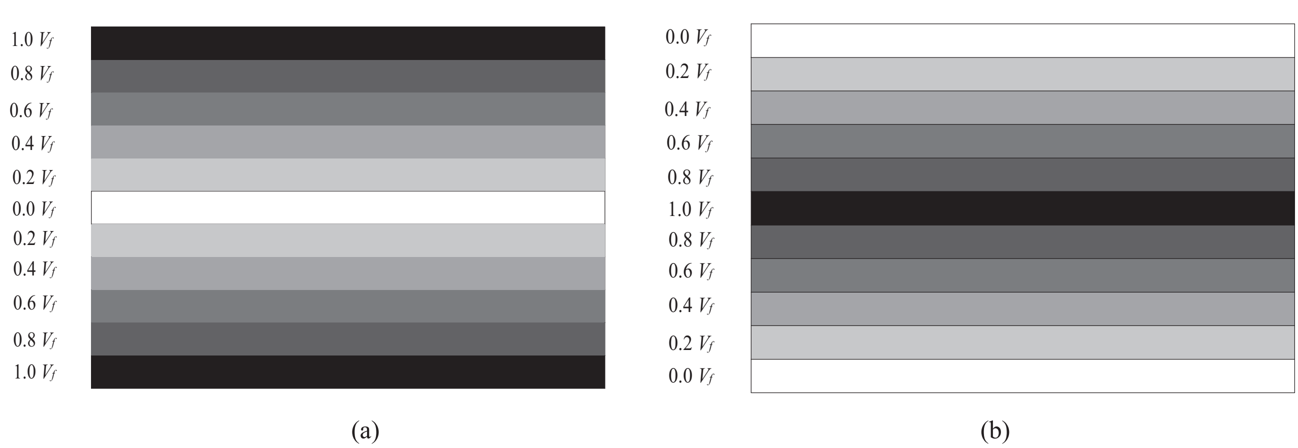

Fig. 3. Stepped functionally graded (a) BFB (b) FBF stacking sequence.

Table 1
Material properties corresponding to different volume fraction V_f of $BaTiO_3$ – $CoFe_2O_4$ (Kondaiah et al. [48]; Wang and Pan [34]).

Material property	Material constants	0 V_f	0.2 V_f	0.4 V_f	0.5 V_f	0.6 V_f	0.8 V_f	1 V_f
Elastic constants (GPa)	$C_{11} = C_{22}$	286	250	225	220	200	175	166
	C_{12}	173	146	125	120	110	100	77
	$C_{13} = C_{23}$	170	145	125	120	110	100	78
	C_{33}	269.5	240	220	215	190	170	162
	$C_{44} = C_{55}$	45.3	45	45	45	45	50	43
	C_{66}	56.5	52	50	50	45	37.5	44.5
Piezoelectric constants (C/m^2)	e_{31}	0	−2	−3	−3.5	−3.5	−4	−4.4
	e_{33}	0	4	7	9.0	11	14	18.6
	e_{15}	0	0	0	0	0	0	11.6
Dielectric constant (10^{-9} C^2/Nm^2)	$\varepsilon_{11} = \varepsilon_{22}$	0.08	0.33	0.8	0.85	0.9	1	11.2
	ε_{33}	0.093	2.5	5	6.3	7.5	10	12.6
Magnetic permeability (10^{-4} Ns^2/C^2)	$\mu_{11} = \mu_{22}$	−5.9	−3.9	−2.5	−2.0	−1.5	−0.8	0.05
	μ_{33}	1.57	1.33	1	0.9	0.75	0.5	0.1
Piezomagnetic constants (N/Am)	q_{31}	580	410	300	350	200	100	0
	q_{33}	700	550	380	320	260	120	0
	q_{15}	560	340	220	200	180	80	0
Magneto-electric constant (10^{-12} Ns/VC)	$m_{11} = m_{22}$	0	2.8	4.8	5.5	6	6.8	0
	m_{33}	0	2000	2750	2600	2500	1500	0
Pyroelectric constant (10^{-7} C/m^2 K)	p_2	0	−3.5	−6.5	−7.8	−9	−10.8	0
Pyromagnetic constant (10^{-5} C/m^2 K)	τ_2	0	−36	−28	−23	−18	−8.5	0
Thermal expansion coefficient (10^{-6} K^{-1})	$\alpha_1 = \alpha_2$	10	10.8	11.8	12.3	12.9	14.1	15.7
	α_3	10	9.3	8.6	8.2	7.8	7.2	6.4
Density (kg/m^3)	ρ	5300	5400	5500	5550	5600	5700	5800

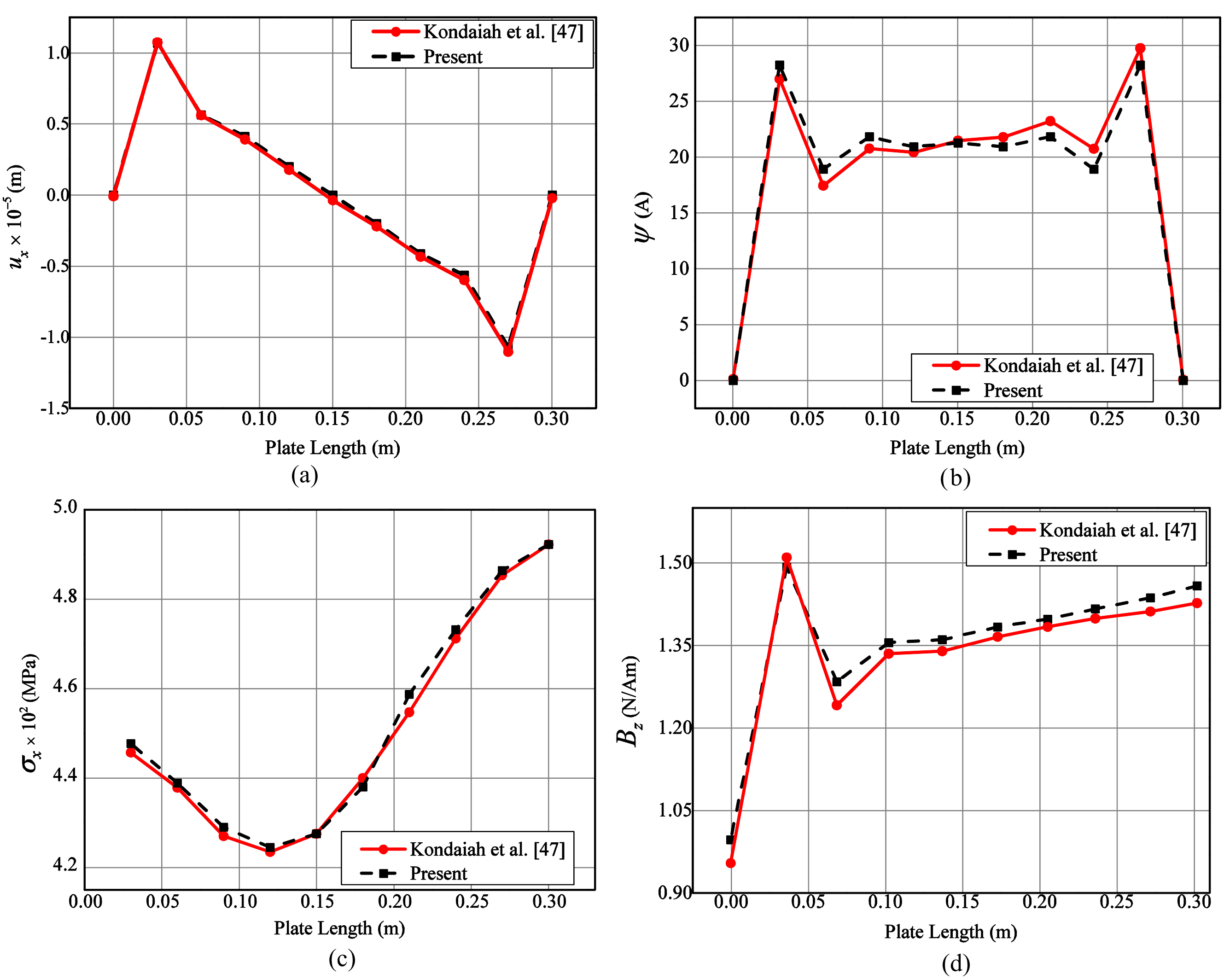

Fig. 4. Verification plots (a) displacement component in x-direction u_x for CCCC MEE plate (b) magnetic potential of CCCC MEE plate (c) normal stress σ_x of CFFC MEE plate (d) magnetic flux density B_z of CFFC MEE plate.

Table 2
Material coefficients of #B and #T materials used in Sladek et al. [33].

Material 1: #B ($\times 10^{10}$ Nm^{-2})		Material 2: #T
$C_{11}^{(1B)}$	10.989	$C_{ij}^{(1T)} = C_{ij}^{(1B)}/2$
$C_{12}^{(1biB)}$	3.297	
$C_{22}^{(1B)}$	10.989	
$C_{66}^{(1B)}$	3.846	
$C_{44}^{(1B)} = C_{55}^{(1B)}$	3.846	

Table 3
Properties of MEE material used in Sladek et al. [33].

Material constants	Values	Material constants	Values
$c_{11} = c_{22}$	22.6×10^{10} Nm^{-2}	d_{33}	350 NA^{-1} m^{-1}
c_{12}	12.4×10^{10} Nm^{-2}	d_{15}	275 NA^{-1} m^{-1}
c_{33}	21.6×10^{10} Nm^{-2}	α_{11}	5.367×10^{-12} Ns (VC)$^{-1}$
c_{66}	5.1×10^{10} Nm^{-2}	α_{33}	2737.5×10^{-12} Ns (VC)$^{-1}$
$c_{44} = c_{55}$	4.3×10^{10} Nm^{-2}	γ_{11}	297 Wb (Am)$^{-1}$
$e_{31} = e_{32}$	-2.2 cm^{-2}	γ_{33}	83.5 Wb (Am)$^{-1}$
e_{15}	5.8 cm^{-2}	ρ	7500 kg m^{-3}
h_{33}	6.35×10^{-9} C(Vm^{-1})		
h_{11}	5.64×10^{-9} C(Vm^{-1})		
$d_{31} = d_{32}$	290.2 NA^{-1} m^{-1}		

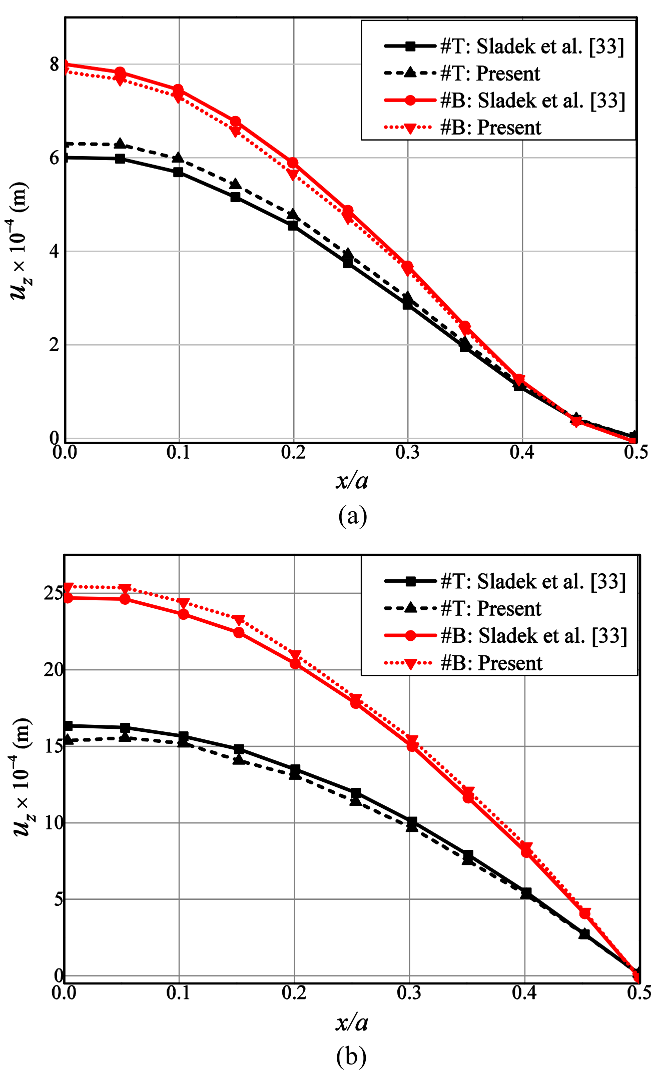

Fig. 5. Verification of transverse displacement component u_z of (a) clamped two layered plate (b) simply supported two layered plate with Sladek et al. [33].

Table 4
Comparison study of the direct quantities of E-FGM MEE plate.

$k = 0$	Present FEM	Wang and Pan [34]	% Error
u_x (10^{-14} m)	26.26	27.13	3.24
u_y (10^{-14} m)	−26.25	−27.13	3.24
u_z (10^{-14} m)	356.2	346.8	−2.71
l (10^{-3} V)	1.69	1.65	−2.42
ψ (10^{-7} A)	−14.03	−13.66	−2.64

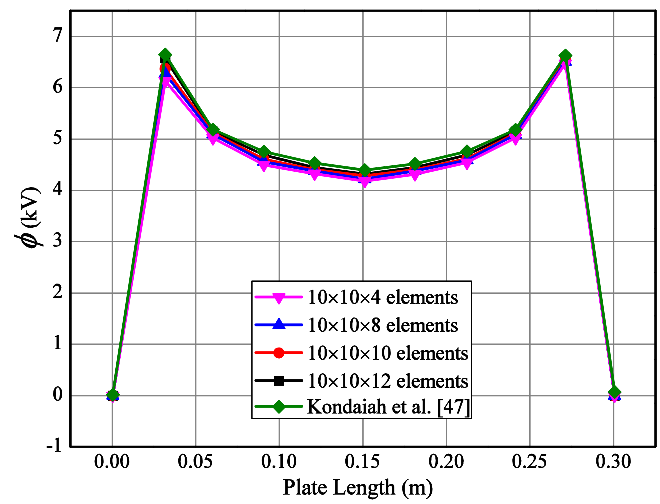

Fig. 6. Convergence of electric potential ϕ.

2.7. Uniform temperature profile

The temperature of the *SFG*-MEE plate is uniformly raised from a stress-free temperature θ_0 to the final temperature θ_{max}. For the ease of calculation, θ_0 is assumed to be 0 *K*. The general temperature variation relation can be written as

$$\Delta\theta = \theta_{max} - \theta_0 \tag{16}$$

2.8. Linear temperature profile

The *SFG*-MEE plate is subjected to a temperature distribution which varies linearly across the plate thickness. The general equation represented by

$$\Delta\theta = \theta_i + \theta_{max}(z/h) \tag{17}$$

where, θ_i is the temperature at the bottom layer of the plate

2.9. Bi-triangular temperature profile

The temperature distribution varies in the form of a tent shape across the plate thickness. It can be explicitly represented as follows:

$$\begin{aligned} \Delta\theta &= \theta_{max}(1 - z) \quad 0 \leqslant z \leqslant h/2 \\ \Delta\theta &= \theta_{max}(z) \quad h/2 \leqslant z \leqslant h \end{aligned} \tag{18}$$

2.10. Parabolic temperature profile

The temperature distribution varying parabolically across the *SFG*-MEE plate thickness can be represented as follows:

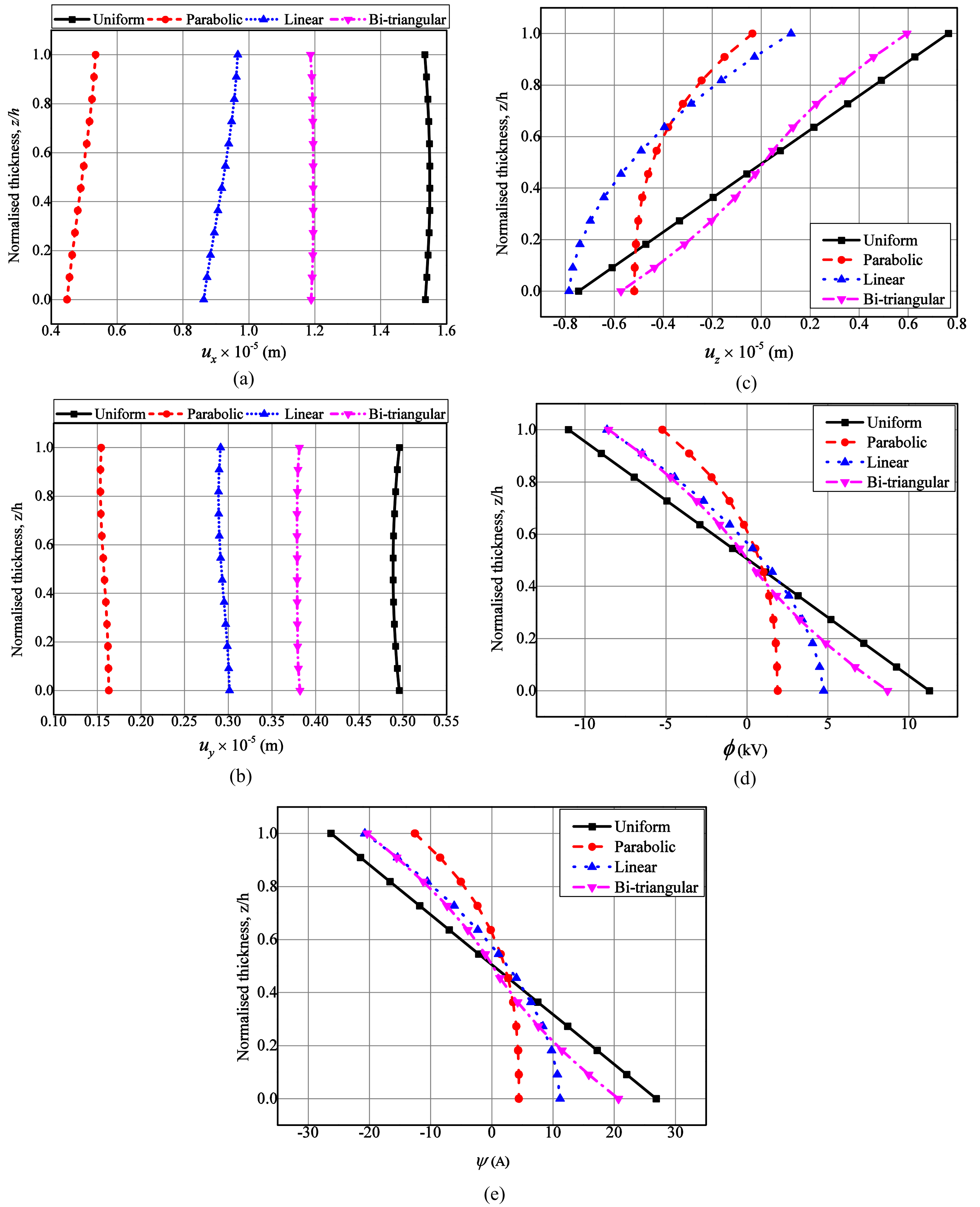

Fig. 7. Effect of temperature distributions on (a) displacement component u_x (b) displacement component u_y (c) displacement component u_z (d) electric potential ϕ (e) magnetic potential ψ.

$$\Delta\theta = \theta_{max}\left\{1 - \left(\frac{z}{h}\right)^2\right\} 0 \leqslant z \leqslant h \tag{19}$$

In the Eqs. (16)–(19) θ_{max} is the maximum temperature, z is the distance of the point of interest from the bottom of the plate and h is the plate thickness.

3. Results and discussion

The effect of various temperature distributions on the direct and derived parameters of the *SFG*-MEE plate is evaluated using the FE formulation derived in the previous section. The *SFG*-MEE plate dimensions considered for the analysis are the length of the plate $a = 0.3$ m, width $b = 0.3$ m and the thickness $h = 0.006$ m. The boundary conditions considered for the *SFG*-MEE plate is illustrated in Fig. 2(a)–(e). By reducing the present FE model for multilayered MEE plate to a single layer MEE plate, the results are verified with those established by Kondaiah et al. [47]. To this end, the material properties tabulated in Table 1 (Kondaiah et al. [48]) are considered in the present analysis. It is evident from Fig. 4(a)–(e) that an excellent agreement is obtained based on the present FE formulation. Further justification for the correctness of the FE formulation is provided by considering two different examples of FG-MEE plate subjected to mechanical loads. At first, a two-layered square plate with indifferent layer thickness illustrated by Sladek et al. [33] is solved with the help of present FE formulation. The bottom layer is assumed to be made of homogeneous properties whereas, the top layer is comprised of MEE material. In addition, two trials are carried out with different material corresponding to the bottom layer. They are represented by *#B* and *#T*, respectively. The material properties corresponding to these homogeneous layers and MEE material are tabulated in Table. 2 and Table 3, respectively. The boundary conditions and loading parameters of the layered plate are maintained identical to that of Sladek et al. [33]. From Fig. 5 (a) and (b), it can be observed that for both clamped plate and simply supported plate, the results show an excellent agreement with Sladek et al. [33]. Further, the static problem of FG-MEE plate subjected to a sinusoidal mechanical load considered by Wang and Pan [34] is also solved and verified. For the purpose of comparison, the MEE plate made of exponentially functionally graded material (E-FGM) with exponential factor $k = 0$ is considered. The boundary conditions and material properties are chosen identical to Wang and Pan [34]. From Table 4, it can be observed that the present results agree very well with Wang and Pan [34]. Further, the convergence study of the present FE model is depicted in Fig. 6 considering the electric potential ϕ of FCFC MEE plate. It can be observed from this figure that with the mesh size of $10 \times 10 \times 12$ elements, a good convergence of the present FE formulation can be achieved. Further, numerical examples are presented to evaluate the effect of various temperature distributions, boundary conditions, pyroeffects and aspect ratio.

3.1. Effect of temperature loadings

In this section, the influence of through thickness temperature distributions (Eqs. (16)–(19)) on the static parameters of *SFG-BFB* MEE plate is analysed. The MEE plate is considered to be clamped on all the edges. Fig. 7(a)–(c) represent the variation of displacement components u_x, u_y and u_z, respectively. It can be interpreted from these figures that uniform temperature load has a significant influence on the variations of u_x, u_y and u_z across the plate thickness, while parabolic temperature profile has a lesser contribution.

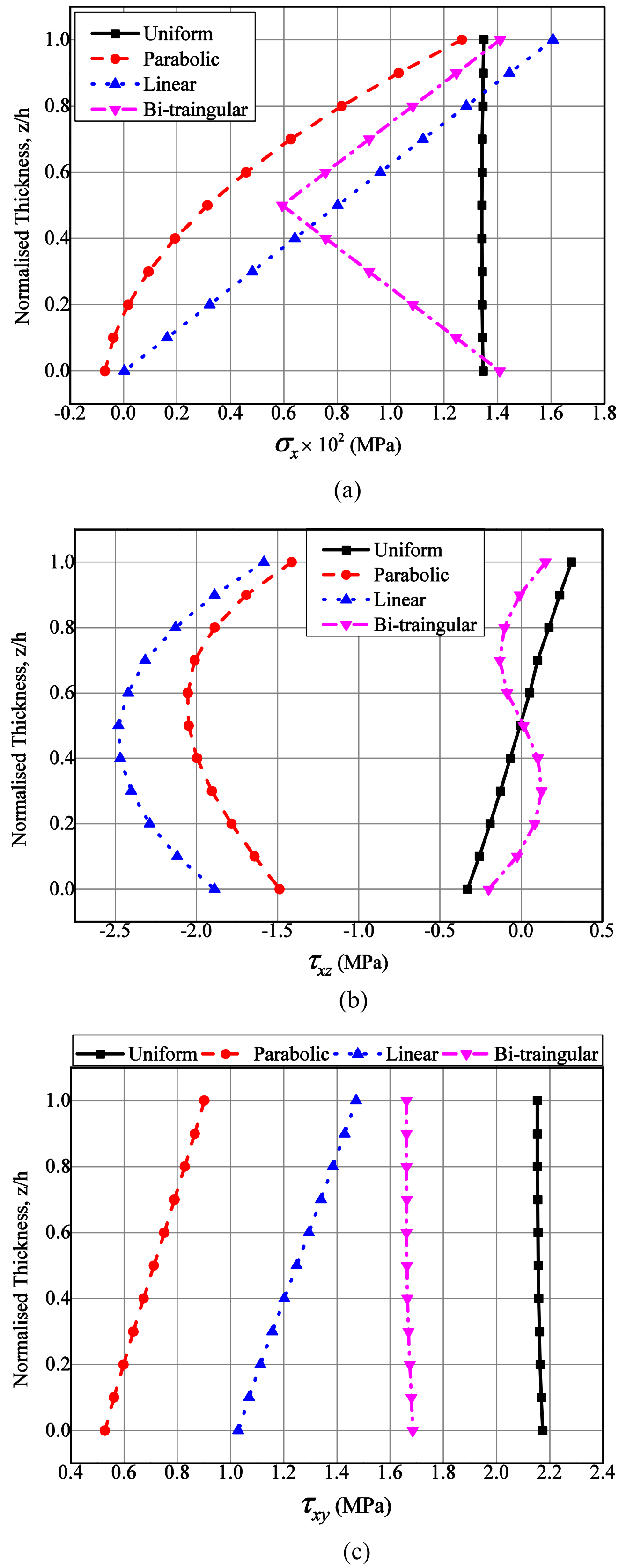

Fig. 8. Effect of temperature distributions on (a) normal stress σ_x (b) shear stress τ_{xz} (c) shear stress τ_{xy}.

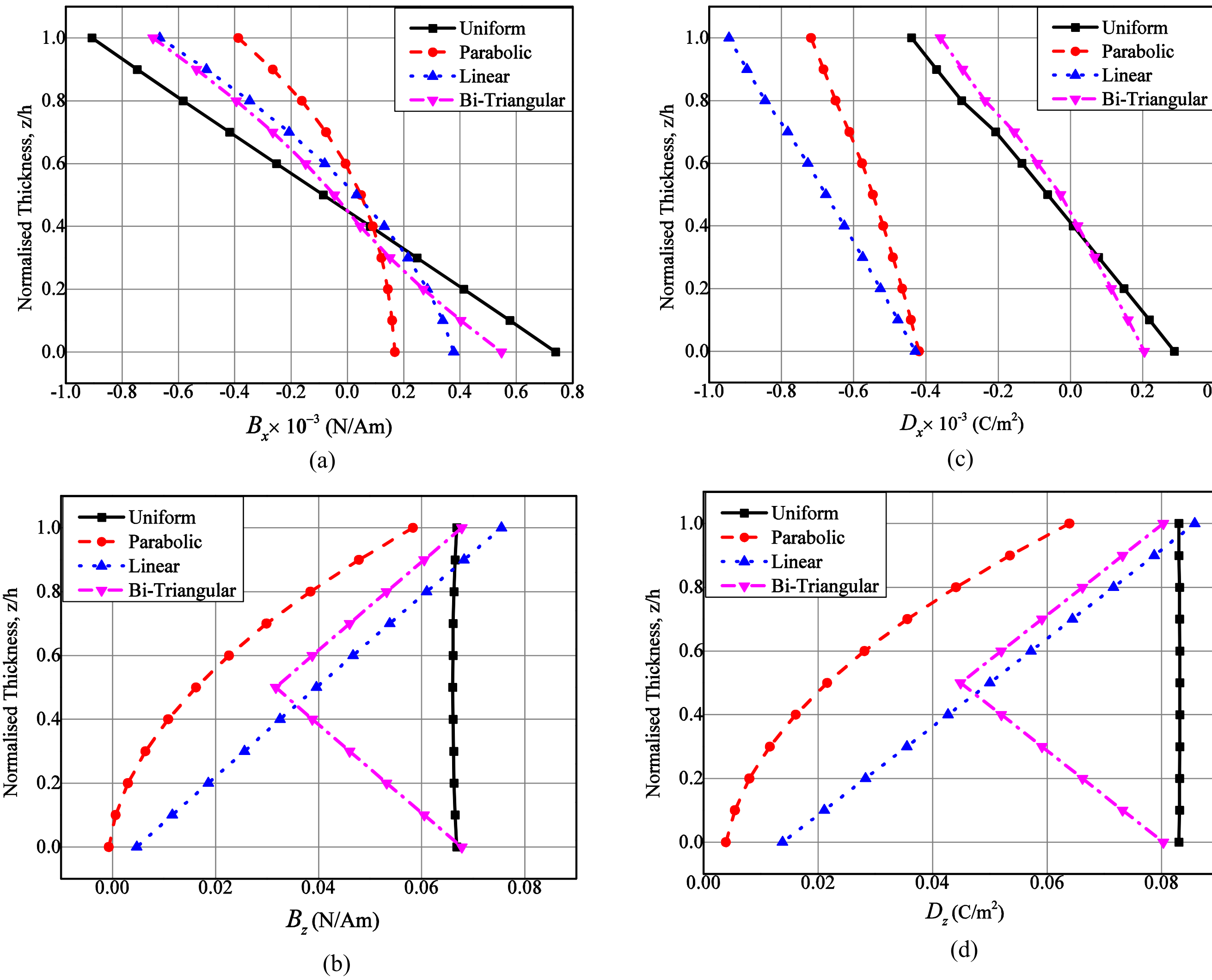

Fig. 9. Effect of temperature distributions on (a) magnetic flux density B_x (b) magnetic flux density B_z (c) electric displacement D_x (d) electric displacement D_z.

Table 5
Effect of stacking sequence on displacement components ($a/h = 50$; $a/b = 1$).

Temperature profile	u_x (10^{-5} m)				u_y (10^{-5} m)				u_z (10^{-6} m)			
	BFB	*FBF*	*SFG-BFB*	*SFG-FBF*	*BFB*	*FBF*	*SFG-BFB*	*SFG-FBF*	*BFB*	*FBF*	*SFG-BFB*	*SFG-FBF*
Uniform	1.41	1.22	1.55	1.36	0.43	0.34	0.5	0.39	7.43	7.11	7.64	7.29
Parabolic	0.44	0.21	0.53	0.32	0.156	0.14	0.16	0.152	5.01	3.6	5.18	4.8
Linear	0.89	0.74	1.0	0.82	0.27	0.18	0.31	0.21	6.87	5.17	7.85	5.68
Bi-triangular	1.02	0.85	1.2	0.93	0.34	0.21	0.38	0.27	5.78	4.98	5.95	5.24

Table 6
Effect of stacking sequence on electric and magnetic potential ($a/h = 50$; $a/b = 1$).

Temperature profile	ϕ (*kV*)				ψ (*A*)			
	BFB	*FBF*	*SFG-BFB*	*SFG-FBF*	*BFB*	*FBF*	*SFG-BFB*	*SFG-FBF*
Uniform	10.17	8.8	11.26	10.69	24.85	26.4	28.45	32.4
Parabolic	3.84	2.89	5.21	4.28	3.845	4.03	4.414	4.68
Linear	6.88	5.67	8.64	7.36	11.14	11.601	12.6	13.80
Bi-triangular	7.16	6.94	8.82	7.88	20.67	22.01	25.84	26.84

Further, the displacement components u_x, u_y and u_z varies symmetrically across the plate thickness for uniform and bi-triangular temperature distributions. In addition, u_z is zero at the midlayer of *SFG-BFB* MEE plate for these two temperature profiles, Meanwhile, for linear and parabolic temperature profile u_x is maximum at the top layer whereas u_y and u_z are found to be higher in the bottom layer of the stacking sequence. This may be attributed to the corresponding temperature distribution. Considering Fig. 7(d), the uniform temperature rise results in a linear variation of the electric potential ϕ across the plate thickness whereas, the symmetric variation is observed for bi-triangular temperature distribution. Also, one can draw the same conclusion with respect to magnetic potential ψ distribution as shown in Fig. 7(e). It is worth noting that for the uniform and bi-triangular temperature profiles, the electric potential and magnetic potential are zero at the mid layer of the *SFG*-MEE plate. The study is extended to evaluate the influence of various through temperature distributions on the derived quantities. It may be noticed from the results plotted in Fig. 8(a) that the normal stress σ_x varies accordingly with the temperature distribution. For the uniform temperature rise, the normal stress σ_x remains almost constant across the plate thickness. Likewise, for a bi-triangular temperature distribution, the maximum σ_x is witnessed at the midplane of the *SFG*-MEE plate. It is interesting to say that irrespective of temperature profile, the maximum normal stress σ_x is noticed at the top layer of SFG-BFB MEE plate. The possible reason may be due to the appearance of highest temperature at the top layer for the corresponding temperature profile. Also, it can be deduced that among all the through thickness temperature distributions considered, a predominant effect of the uniform temperature distribution prevails on σ_x. This may be due to the development of constant pyroloads generated through the thickness of *SFG-BFB* MEE plate. From Fig. 8(b), a significant effect of linear temperature distribution is noticed with respect to the variation of shear stress component τ_{xz}. Moreover, at the midplane of *SFG*-MEE plate, the maximum value of τ_{xz} is noticed for linear temperature distribution and parabolic temperature distribution, whereas for the bi-triangular and uniform temperature distribution, it is found to be the minimum. The variation of stress component τ_{xy} across the plate thickness is depicted in Fig. 8(c), while Fig. 9(a) and (b) display the variation of magnetic flux density components B_x and B_z, respectively. It is clearly seen from Fig. 9(c) and (d) that the linear temperature distribution has a significant influence on D_x which is followed by the parabolic, uniform, and bi-triangular temperature profiles. But, the uniform temperature distribution exhibits a predominant effect on D_z.

3.2. Effect of stacking sequence

It is observed from the literature review that the MEE plate with three layered stacking sequence is the most investigated configuration having either *B/F/B* or *F/B/F* arrangement. Here, *B* label and *F* label corresponds to pure piezoelectric phase ($BaTiO_3$) and pure piezomagnetic phase ($CoFe_2O_4$), respectively. In addition, the effect of intermediate volume fraction of $BaTiO_3$ and $CoFe_2O_4$ are neglected in most of the available literatures. Since, in the present analysis the through thickness temperature profiles are considered, the different values of temperature encounters with the material properties corresponding to the different volume fraction of $BaTiO_3$ and $CoFe_2O_4$. This leads to indifferent coupling effects across the plate thickness, exhibiting a direct impact on the static parameters of SFG-MEE plate. Therefore, examining the influence of stacking sequence on the coupled response of *SFG*-MEE plate is of prime importance. As tabulated in Table 5, it can be noticed that the displacement components u_x, u_y and u_z are higher for *SFG-BFB* MEE plate. However, as expected, the electric potential and magnetic potential are higher for *SFG-BFB* and *SFG-FBF* MEE plates, respectively, as tabulated in Table 6. This may be attributed to the influence of pyroelectric and pyromagnetic coupling effects with the corresponding stacking sequences. In addition, the presence of more number of pure piezoelectric and piezomagnetic layers also plays a major role. The results from Table 7 suggest that for all the temperature profiles, a minimum stress is observed for

Table 7
Effect of stacking sequence on normal stress $\boldsymbol{\sigma_x}$ (*a/h* = 50; *a/b* = 1).

Temperature profile	$\sigma_x \times 10^8$(Pa)			
	BFB	*FBF*	*SFG-BFB*	*SFG-FBF*
Uniform	2.80	2.77	1.35	1.30
Parabolic	2.58	1.73	1.27	0.87
Linear	2.89	2.70	1.61	1.27
Bi-triangular	3.28	2.83	1.4	1.36

Table 8
Effect of stacking sequence on magnetic flux density components (*a/h* = 50; *a/b* = 1).

Temperature profile	B_x (N/Am)				B_y (N/Am)				B_z (N/Am)			
	BFB ($\times 10^{-4}$)	*FBF* ($\times 10^{-2}$)	*SFG-BFB* ($\times 10^{-3}$)	*SFG-FBF*	*BFB* ($\times 10^{-4}$)	*FBF* ($\times 10^{-2}$)	*SFG-BFB* ($\times 10^{-3}$)	*SFG-FBF*	*BFB*	*FBF*	*SFG-BFB*	*SFG-FBF*
Uniform	7.21	11.1	0.91	1.3	7.04	11.3	0.91	1.4	0.07	2.42	0.066	2.58
Parabolic	1.15	1.9	0.37	0.2	1.13	2.51	0.38	0.25	0.04	2.1	0.058	1.49
Linear	3.10	5.19	0.65	0.5	3.03	5.58	0.66	0.6	0.06	2.73	0.075	2.37
Bi-triangular	5.71	8.31	0.7	1.1	5.59	8.45	0.69	1.1	0.069	2.45	0.067	2.61

Table 9
Effect of stacking sequence on electric displacement components (*a/h* = 50; *a/b* = 1).

Temperature profile	D_x (C/m^2)				D_y (C/m^2)				D_z (C/m^2)			
	BFB ($\times 10^{-4}$)	*FBF* ($\times 10^{-7}$)	*SFG-BFB* ($\times 10^{-4}$)	*SFG-FBF* ($\times 10^{-7}$)	*BFB* ($\times 10^{-4}$)	*FBF* ($\times 10^{-7}$)	*SFG-BFB* ($\times 10^{-3}$)	*SFG-FBF* ($\times 10^{-7}$)	*BFB* ($\times 10^{-2}$)	*FBF* ($\times 10^{-4}$)	*SFG-BFB* ($\times 10^{-2}$)	*SFG-FBF* ($\times 10^{-4}$)
Uniform	2.51	18.9	4.4	20.4	2.47	17.6	4.33	20	7.92	3.18	8.32	3.14
Parabolic	2.59	2.1	7.2	3.82	2.20	1.87	6.6	3.81	4.12	1.62	6.39	2.39
Linear	3.18	5.89	9.45	8.1	2.66	5.27	8.8	8	6.74	2.67	8.58	3.22
Bi-triangular	1.91	1.42	3.6	1.43	1.94	13.2	3.5	14.1	7.72	3.08	8.03	3.02

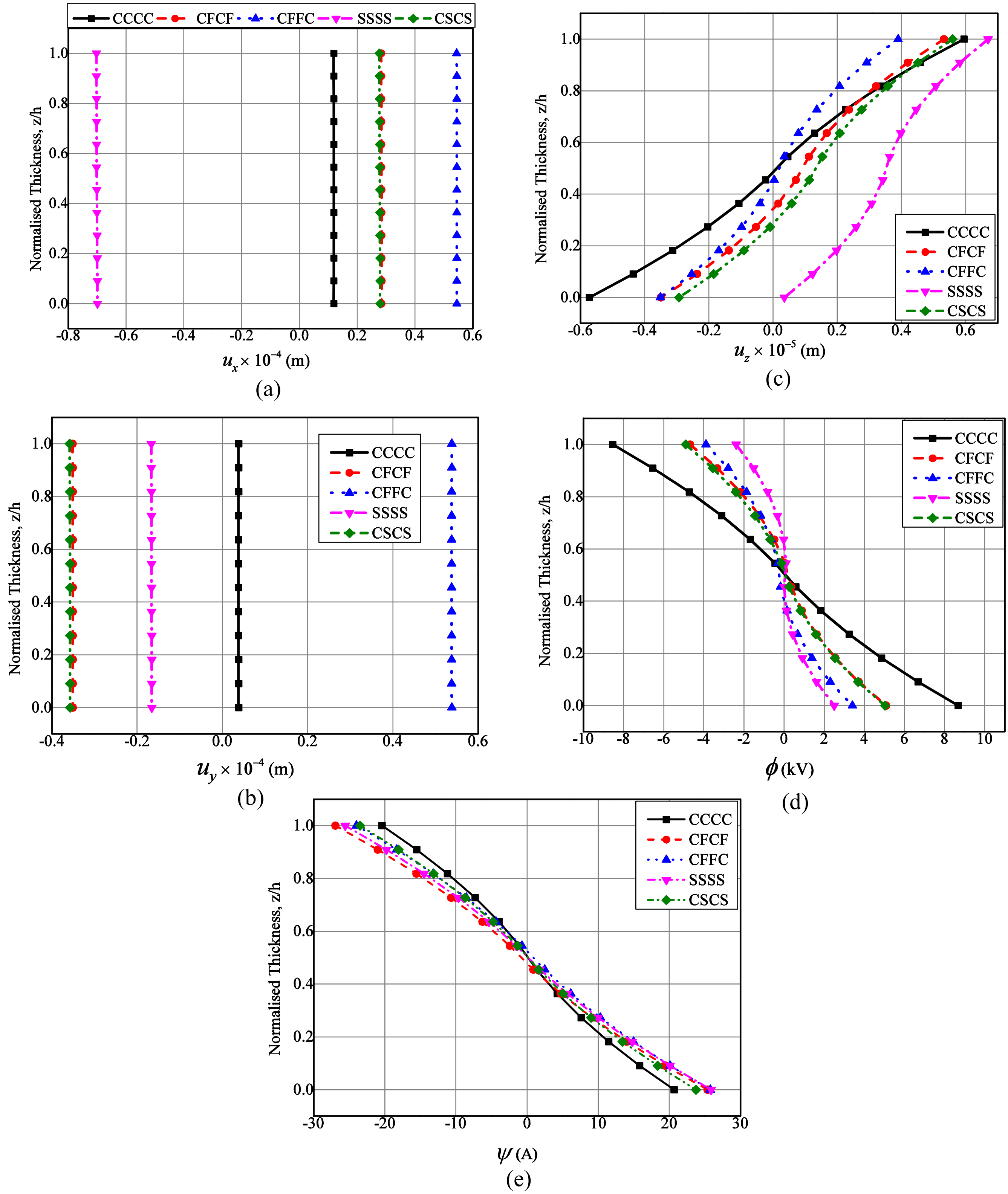

Fig. 10. Effect of boundary condition on (a) displacement component u_x (b) displacement component u_y (c) displacement component u_z (d) electric potential ϕ (e) magnetic potential ψ.

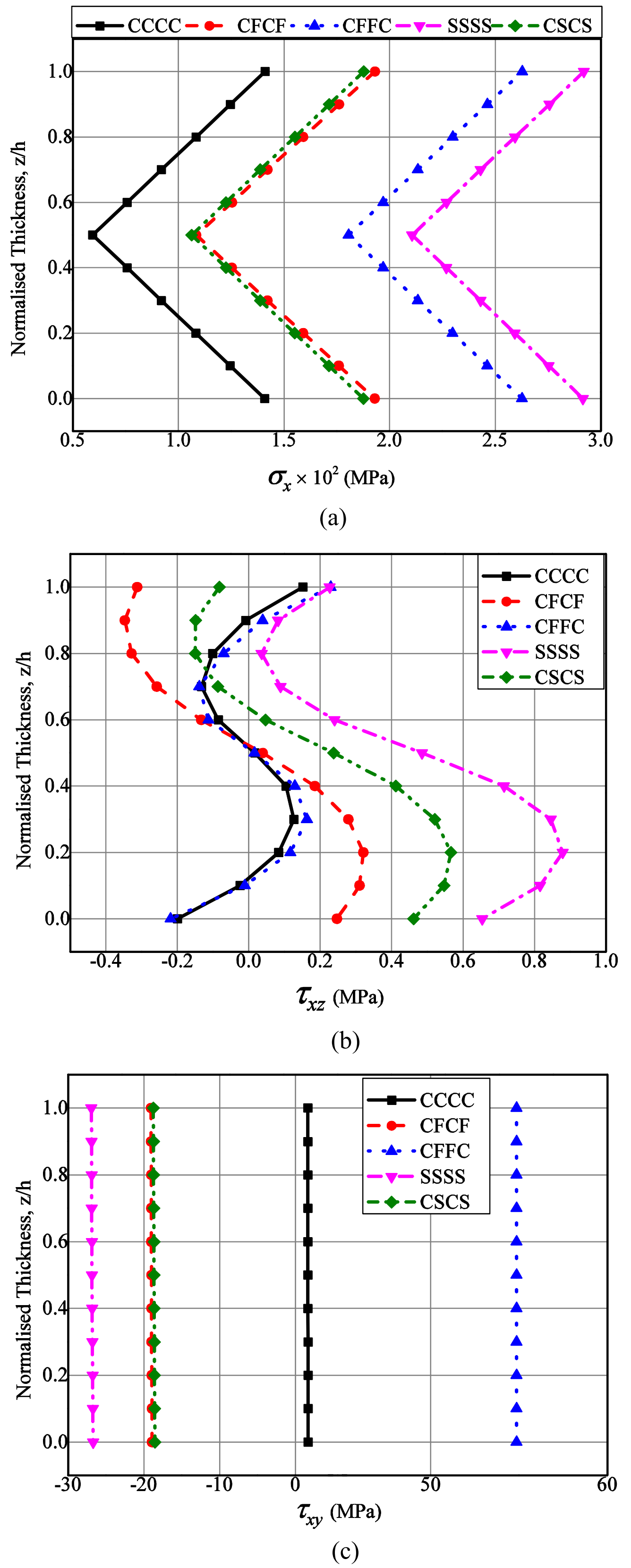

Fig. 11. Effect of boundary condition on (a) normal stress σ_x (b) shear stress τ_{xz} (c) shear stress τ_{xy}.

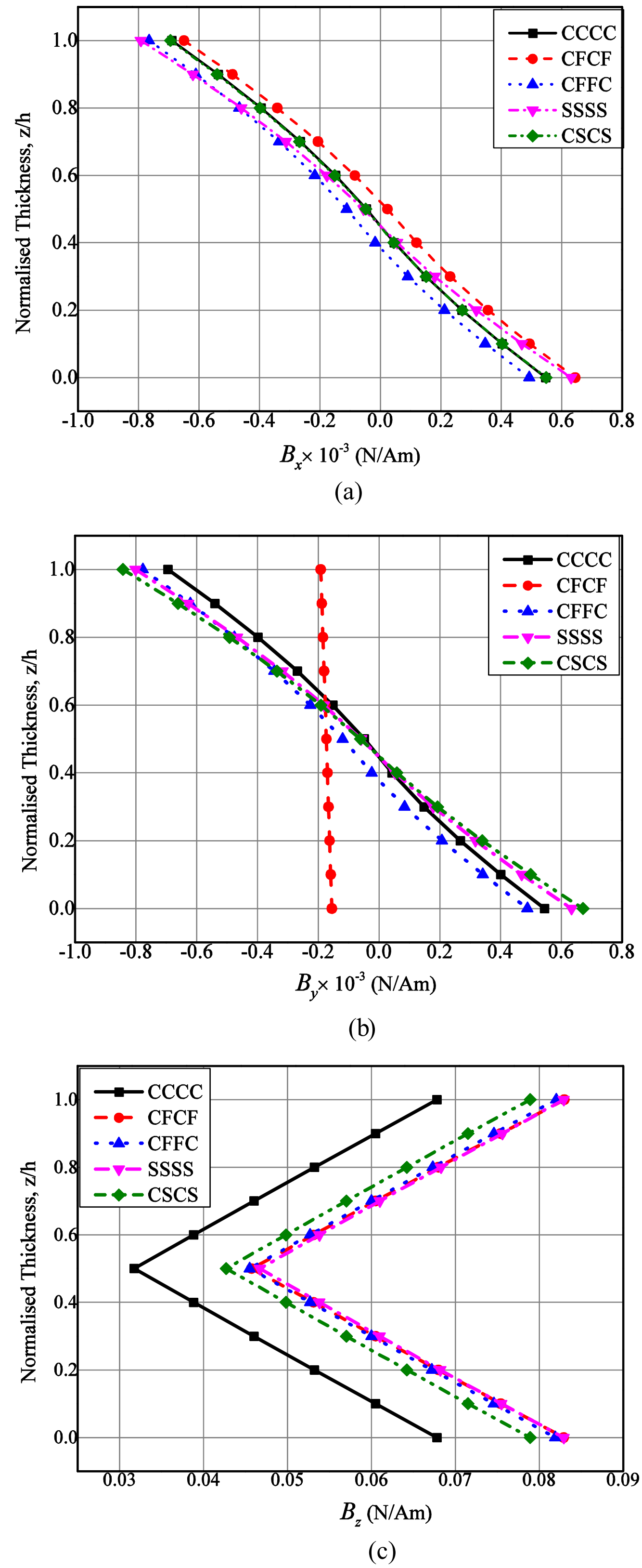

Fig. 12. Effect of boundary conditions on (a) magnetic flux density B_x (b) magnetic flux density B_y (c) magnetic flux density B_z.

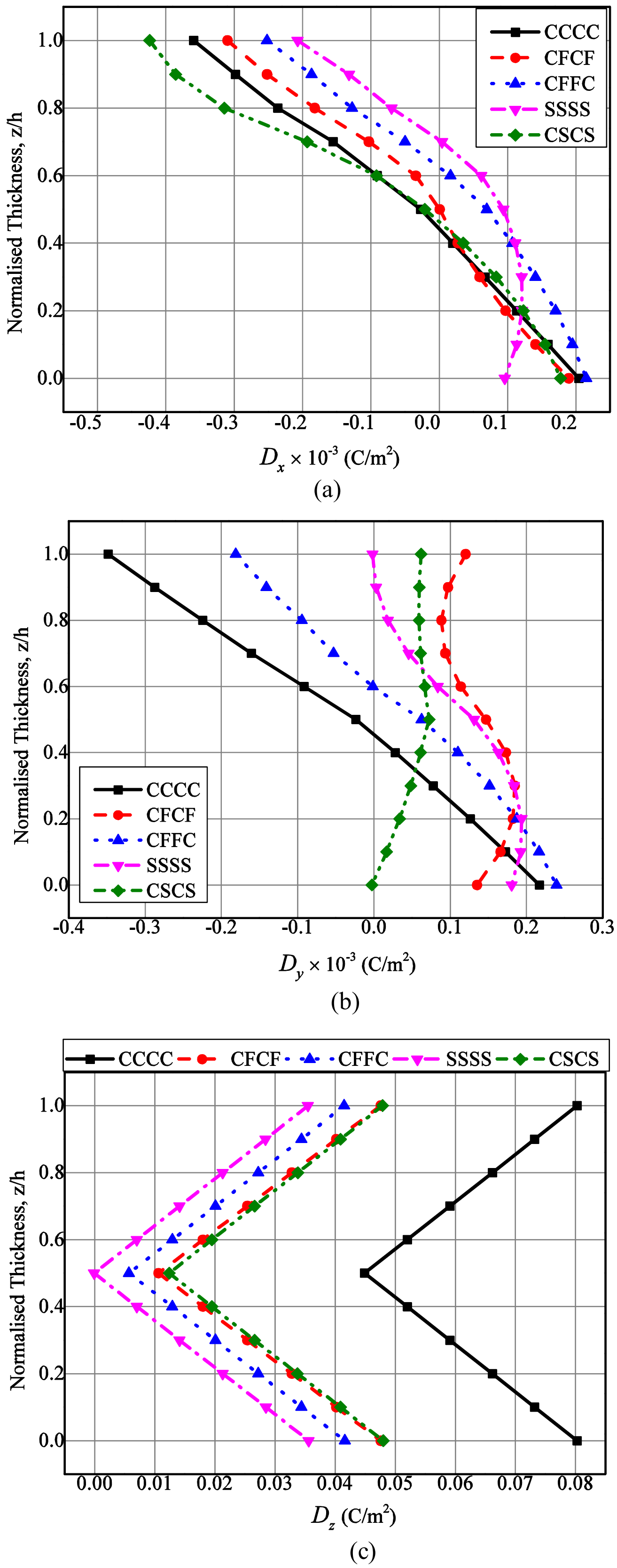

Fig. 13. Effect of boundary conditions on (a) electric displacement D_x (b) electric displacement D_y (c) electric displacement D_z.

SFG-FBF MEE plate. From Table 8 and Table 9, a significant influence of the *SFG-FBF* and *SFG-BFB* MEE plate is observed on the magnetic flux density components (B_x, B_y and B_z) and electric displacement components (D_x, D_y and D_z), respectively. It may be due to the fact that the electric potential and magnetic potential has a direct effect on the electric displacements and magnetic flux density components, respectively. In contrast to conventional three layered MEE plate, the *SFG*-MEE stacking sequence results in higher displacements components and lower stress components which are highly desirable in the design of smart structures. Hence, from the comprehensive investigation carried out here, one can explicitly confirm that the stepped functionally graded magneto-electro-elastic (*SFG*-MEE) plate results in a superior performance in comparison with the conventional three-layered MEE plate.

3.3. Effect of boundary condition

The effect of various boundary conditions (see Fig. 2(a)–(e)) on the direct and derived quantities of *SFG-BFB* MEE plate is investigated by considering the bi-triangular temperature distribution in the analysis. It can be pointed out from Fig. 10(a) that u_x is higher for SSSS MEE plate as compared to other boundary conditions. This may be attributed to the free movement of the plate in *x*- direction. Further, the displacement component u_y and u_z are higher for CFFC and CCCC MEE plate as shown in Fig. 10 (b) and (c), respectively. The distribution of electric potential for various boundary conditions is represented in Fig. 10(d). It can be observed from this figure that CCCC boundary edge has a significant effect on the electric potential while SSSS boundary edge exhibits a minimal effect. In contrast to other boundary edges, a dominant effect of CFCF boundary edge on the magnetic potential is witnessed as indicated in Fig. 10(e). Furthermore, a significant influence of CCCC boundary condition is noticed on the variation of normal stress component σ_x as shown in Fig. 11(a). For all the boundary conditions, the maximum value of σ_x is witnessed at the midplane of the *SFG*-MEE plate. It may be due to the fact that the temperature is higher at the midspan. It may also be noticed from Fig. 11(b) that a substantial effect of SSSS boundary condition is noticed on τ_{xz} while CFFC boundary condition has a significant effect on τ_{xy} as depicted in Fig. 11(c). Fig. 12(a)–(c) illustrate the distribution of B_x, B_y, and B_z, respectively. From these figures, it may be observed that the SSSS boundary condition has a predominant influence on the variation of B_x and B_z. In addition, it is also noticed that the CFCF MEE plate results a minimum B_y. The numerical evaluation is extended to compute D_x, D_y, and D_z. From Fig. 13 (a)–(c), it is observed that in contrast to other boundary conditions, CCCC MEE plate results in a higher electric displacement.

3.4. Effect of aspect ratio (a/h)

The effect of aspect ratio (a/h) on *SFG-BFB* MEE plate subjected to uniform temperature load is evaluated. The clamped boundary condition is enforced on all the edges of the plate. In order to clearly distinguish between the effect of thin and thick *SFG-BFB* MEE plates, different values of aspect ratios (a/h) have been considered for the analysis. Fig. 14(a)–(e) illustrate the influence of aspect ratio on the displacement components (u_x, u_y and u_z), electric potential ϕ, and magnetic potential ψ, respectively. It can be inferred from these figures that *SFG-BFB* MEE plate with lower aspect ratio results in a greater value of u_x, u_y and u_z. However, in contrast to u_x and u_y a marginal effect of aspect ratio is witnessed on u_z. The further numerical study reveals that the thick plate has a predominant effect on the potentials (ϕ and ψ) of the system. Meanwhile, it is found that the stresses are greatly affected by the aspect ratios considered. As the *SFG-BFB* MEE plate becomes thinner, the normal stress σ_x drastically reduces across the plate

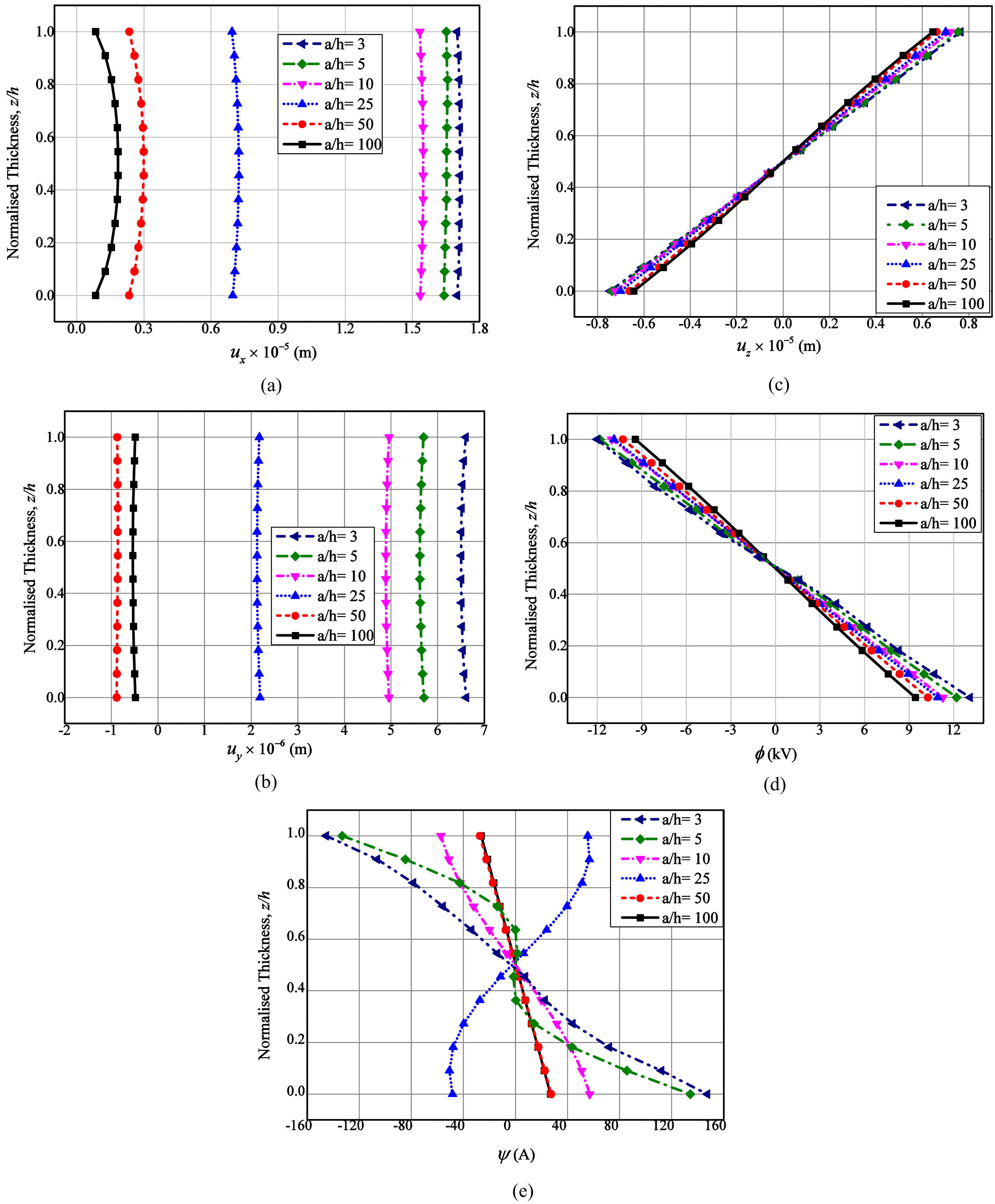

Fig. 14. Effect of aspect ratio (a/h) on (a) displacement component u_x (b) displacement component u_y (c) displacement component u_z (d) electric potential ϕ (e) magnetic potential ψ.

thickness as illustrated in Fig. 15(a). Analogously, a similar trend of variation is followed by the shear stress components τ_{xz}, τ_{xy}, and τ_{yz} as elucidated in Fig. 15(b)–(d), respectively. The numerical evaluation is further extended to interpret the influence of different temperature profile on *SFG-BFB* MEE plate for various aspect ratios. It can be noticed from Table 10 that irrespective of the temperature distribution considered, the effect of *a/h* ratios on the displacement u_z and stress components remains unchanged. In other words, thick plate (*a/h* = 3) has a significant effect on the direct quantities and stress components. Likewise, the results presented in Table 11 suggest that for all forms of temperature loads, a thin plate (*a/h* = 100) yields lower electric displacement components (D_x, D_y and D_z) and magnetic flux density components (B_x, B_y and B_z) of *SFG*-MEE plate (Figs. 16 and 17).

3.5. Effect of length-to-width ratio (a/b)

The numerical evaluation is carried out to explore the effect of the length-to-width ratio (*a/b*) on the static parameter of *SFG*-MEE plate. The present analysis considers the plate is thick (*a/h* = 5) and it is clamped on all the edges (Fig. 2a). The variation of direct quantities such as u_x, u_y, u_z, ϕ and ψ with respect to different *a/b* ratio is plotted in Fig. 18(a)–(e), respectively. As elucidated in these figures, the displacement components u_x, u_y and u_z exhibit a decreasing trend as *a/b* ratio increases. Meanwhile, the electric potential and magnetic potential increases with the increase in the *a/b* ratio. However, it is worth stating that for the higher values of *a/b* ratio, the discrepancy becomes negligible for u_z and ϕ. The variation of normal stress σ_x and shear stress τ_{xz} along the plate thickness is shown in Fig. 19(a) and (b), respectively. The observation from Figs. 20 and 21 reveal that for *a/b* = 2, a drastic increase in the electric displacement components (D_x, D_y and D_z) and magnetic flux density components (B_x, B_y and B_z) is witnessed. In other words, for the given aspect ratio (*a/h*), higher *a/b* ratio tends to increase the electric displacement and magnetic flux density components along the thickness of *SFG*-MEE plate. Further, Table 12 depicts the maximum values of direct quantities such as u_z, ϕ and ψ for different combinations of aspect ratio, the length-to-width ratio (*a/b*) and temperature profiles. The results from this table suggest that irrespective of the temperature profiles, lower *a/h* ratio and *a/b* ratio results in a higher value of u_z whereas, the combination of lower aspect ratio (*a/h*) and higher of length-to-width ratio (*a/b*) yields the maximum value of the direct quantities.

3.6. Influence of product properties

It is familiar that the MEE material displays an additional thermo-electric (pyroelectric effect) and thermo-magnetic (pyro-

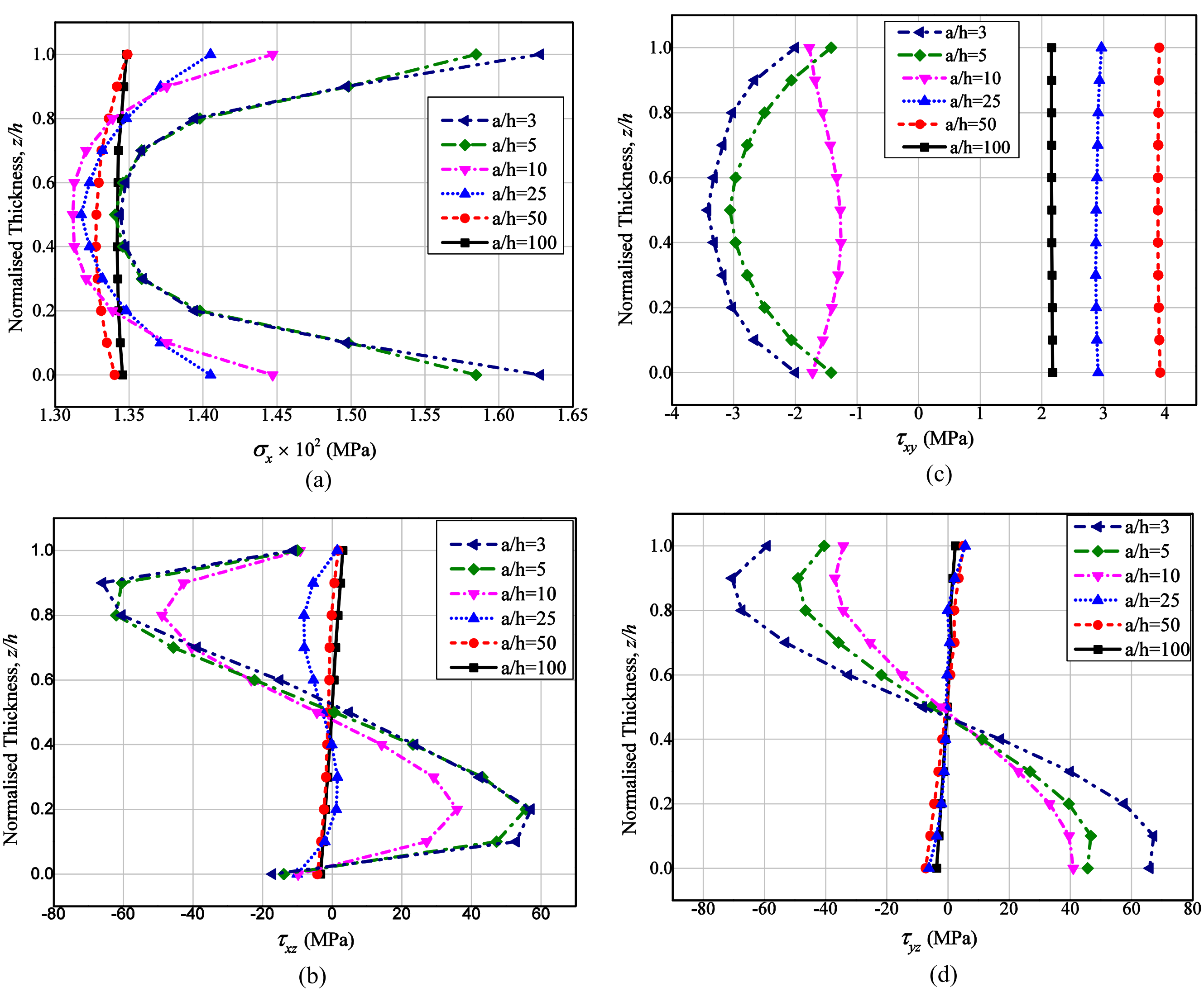

Fig. 15. Effect of aspect ratio (*a/h*) on (a) normal stress σ_x (b) shear stress τ_{xz} (c) shear stress τ_{xy} (d) shear stress τ_{yz}.

Table 10
Effect of aspect ratio (a/h) on the maximum values of transverse deflection, normal stresses and shear stresses for different temperature profiles.

a/h	Temperature profiles	u_z ($\times 10^{-6}$ m)	σ_x ($\times 10^2$ MPa)	σ_y ($\times 10^2$ MPa)	σ_z ($\times 10^2$ MPa)	τ_{xz} (MPa)	τ_{xy} (MPa)	τ_{yz} (MPa)
3	Uniform	8.16	1.81	1.68	2.74	6.60	3.92	7.06
	Parabolic	5.88	1.35	1.37	2.23	4.22	1.64	2.69
	Linear	8.34	1.84	1.81	2.96	6.62	2.71	4.71
	Bi-Triangular	6.45	1.70	1.64	2.69	4.73	3.03	5.16
5	Uniform	8.09	1.70	1.64	2.71	6.20	3.22	4.90
	Parabolic	5.62	1.32	1.35	2.22	4.17	1.23	2.26
	Linear	8.12	1.79	1.78	2.94	6.37	2.18	3.49
	Bi-Triangular	6.32	1.66	1.61	2.67	4.42	2.37	3.67
10	Uniform	7.95	1.60	1.53	2.64	4.89	3.06	4.10
	Parabolic	5.49	1.27	1.31	2.20	4.13	1.16	2.21
	Linear	8.01	1.69	1.71	2.89	5.73	1.97	2.93
	Bi-Triangular	6.19	1.56	1.54	2.62	3.70	2.30	3.07
25	Uniform	7.78	1.41	1.37	2.58	1.20	2.96	0.72
	Parabolic	5.32	1.25	1.27	2.17	3.97	1.07	2.10
	Linear	7.94	1.61	1.62	2.84	4.93	1.95	2.76
	Bi-Triangular	6.03	1.44	1.42	2.57	1.24	2.29	0.51
50	Uniform	7.64	1.35	1.36	2.56	0.42	2.17	0.62
	Parabolic	5.18	1.22	1.26	2.16	3.50	0.64	1.89
	Linear	7.85	1.59	1.61	2.83	4.20	1.47	2.66
	Bi-Triangular	5.95	1.41	1.41	2.56	0.41	1.69	0.43
100	Uniform	7.46	1.34	1.34	2.55	0.33	1.77	0.37
	Parabolic	5.04	1.20	1.25	2.15	2.05	0.90	1.63
	Linear	7.65	1.57	1.59	2.82	2.48	1.23	1.95
	Bi-Triangular	5.86	1.40	1.39	2.56	0.21	1.33	0.26

Table 11
Effect of aspect ratio (a/h) on the maximum values of electric displacement components and magnetic flux density components for different temperature profiles.

a/h	Temperature profiles	D_x ($\times 10^{-3}$C/m^2)	D_y ($\times 10^{-3}$C/m^2)	D_z ($\times 10^{-3}$C/m^2)	B_x ($\times 10^{-3}$ N/Am)	B_y ($\times 10^{-3}$ N/Am)	B_z ($\times 10^{-3}$ N/Am)
3	Uniform	4.8	2.5	83.1	35.7	1.4	157.3
	Parabolic	1.4	1.4	63.7	15.6	0.59	89.3
	Linear	2.9	2.3	83.1	25.3	0.98	128.6
	Bi-Triangular	3.4	1.8	75.4	30.4	1.1	152.9
5	Uniform	3.1	2.4	83.3	22.6	1.04	119.7
	Parabolic	1.0	1.38	64.2	7.1	0.45	58.2
	Linear	1.9	2.2	83.8	13.9	0.83	83.5
	Bi-Triangular	2.2	1.7	76.4	16.8	0.71	79.2
10	Uniform	1.2	1.9	84.1	88.6	0.80	109.7
	Parabolic	0.9	1.3	64.5	29.2	0.28	49.8
	Linear	1.3	2.01	85.2	53.7	0.56	69.3
	Bi-Triangular	1.1	1.47	77.7	61.1	0.57	81.7
25	Uniform	1.01	0.76	84.3	44.6	1.2	139.4
	Parabolic	0.91	1.27	64.9	13.7	0.45	49.2
	Linear	1.28	1.6	86.4	27.6	0.78	85.1
	Bi-Triangular	0.85	0.71	78.9	31.8	0.85	112.9
50	Uniform	0.44	0.43	83.2	2.03	0.91	66.7
	Parabolic	0.71	0.66	63.9	0.86	0.37	58.1
	Linear	0.95	0.88	85.8	1.5	0.66	75.2
	Bi-Triangular	0.36	0.35	80.3	1.4	0.69	67.6
100	Uniform	0.39	0.37	82.7	0.91	0.92	66.8
	Parabolic	0.65	0.61	63.1	0.39	0.38	58.3
	Linear	0.82	0.76	84.6	0.66	0.67	75.5
	Bi-Triangular	0.32	0.30	79.5	0.69	0.70	67.8

magnetic) coupling in the presence of thermal environment. This distinct property has a beneficial effect on the electric potential of the MEE structures [47]. Alongside, it is found that the pyroeffects are significantly enhanced with functional gradation [52]. Therefore, the investigation of the influence of product properties (pyroeffects) on the static behavior of *SFG-BFB MEE* plate is of high value of significant interest. In this regard, considering different thermal loading profiles, a comparative study is made to analyse the distribution of the electric potential with and without pyroeffects. It can be clearly observed from Fig. 22(a)–(d) that for all the temperature distributions, the pyroeffects tend to improve the electric potential across the thickness of *SFG-BFB* MEE plate. According to Table 13, it can be deduced that irrespective of the temperature profiles and stacking sequences, neglecting the influence of pyroeffects degrades the maximum attainable electric potential. In addition, it is also seen that bi-triangular temperature profile has a higher percentage reduction in the maximum electric potential when the pyroeffects are neglected. It is followed by parabolic, uniform and linear temperature profiles. Furthermore, the contribution of the pyroeffects towards the maximum electric

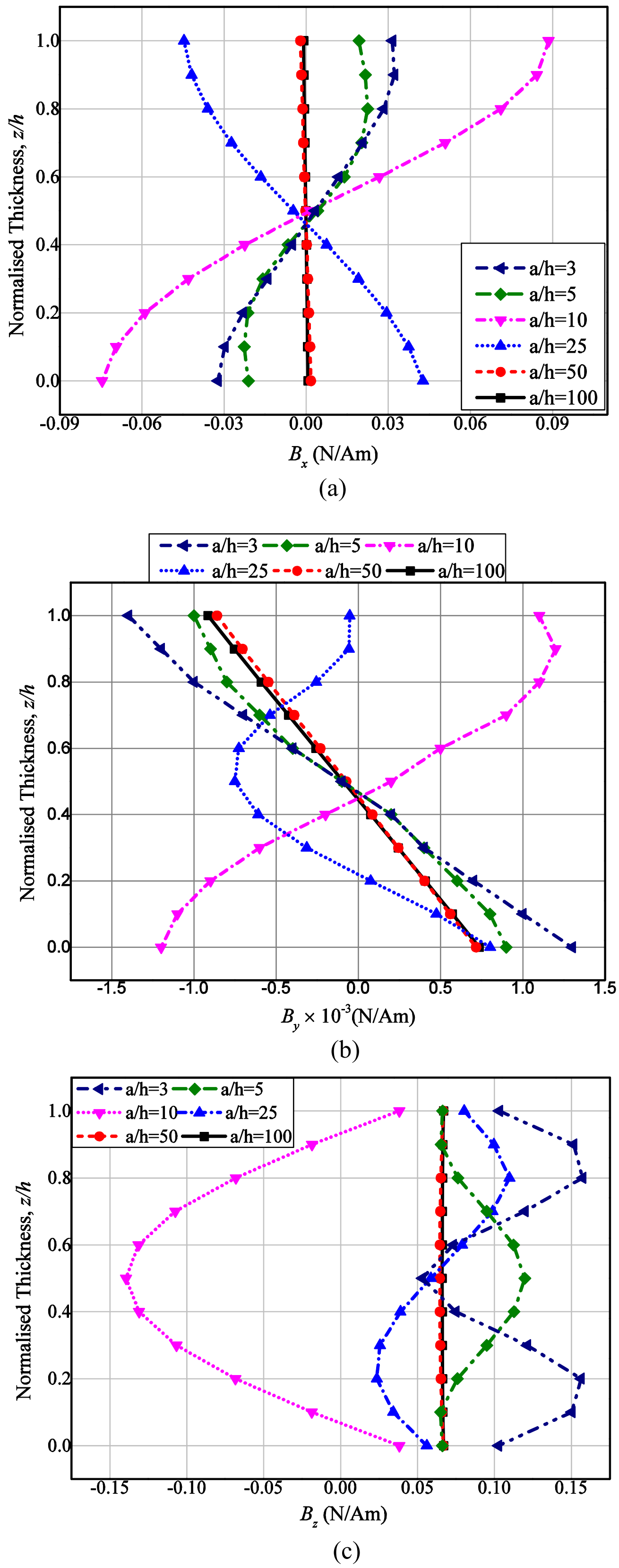

Fig. 16. Effect of aspect ratio (a/h) on (a) magnetic flux density B_x (b) magnetic flux density B_y (c) magnetic flux density B_z.

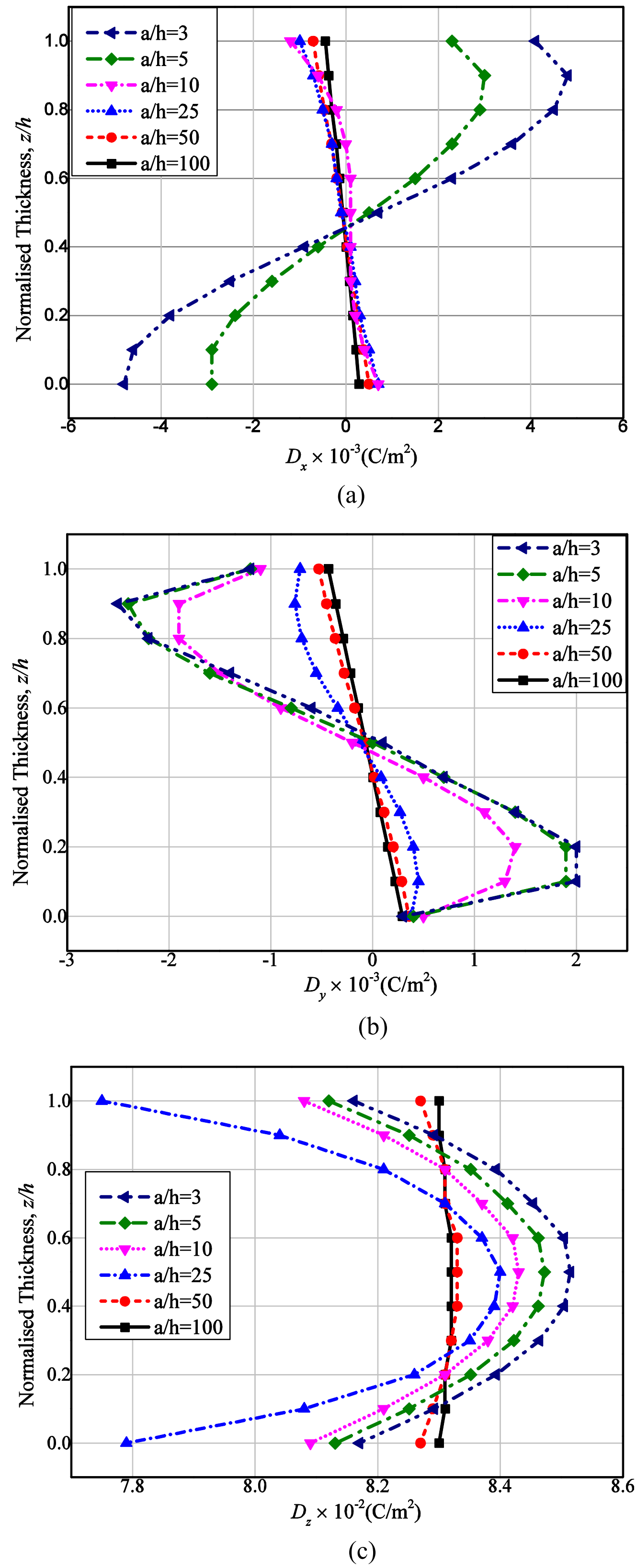

Fig. 17. Effect of aspect ratio (a/h) on (a) electric displacement D_x (b) electric displacement D_y (c) electric displacement D_z.

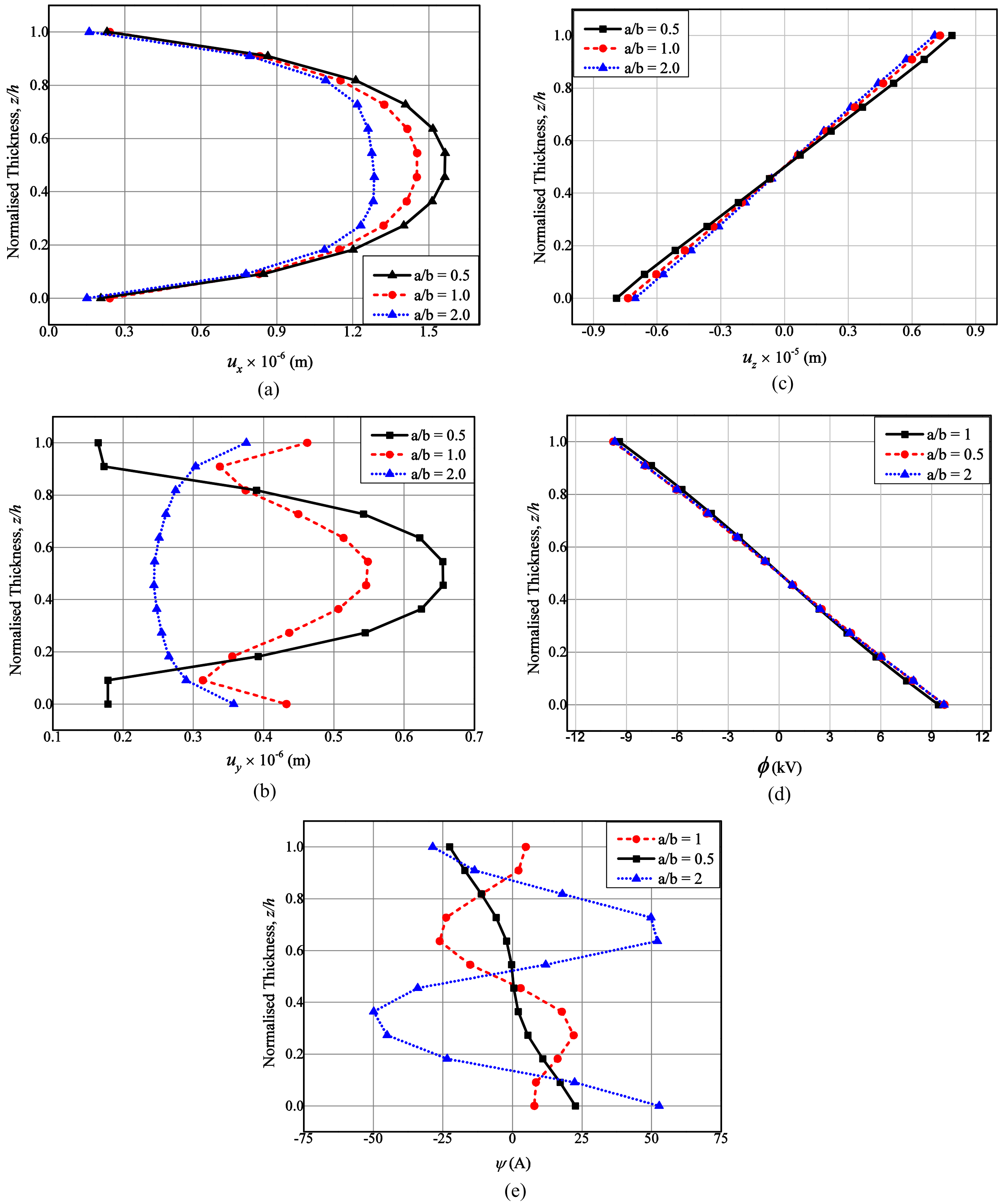

Fig. 18. Effect of length-to-width ratio (a/b) on (a) displacement component u_x (b) displacement component u_y (c) displacement component u_z (d) electric potential ϕ (e) magnetic potential ψ.

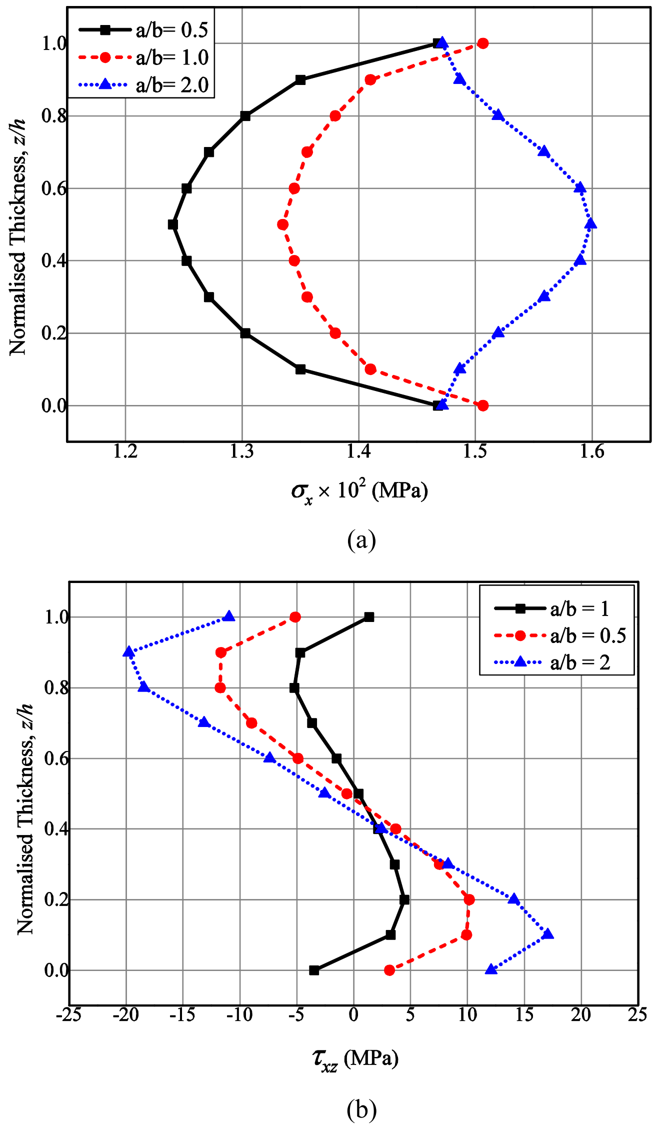

Fig. 19. Effect of length-to-width ratio (a/b) on (a) normal stress σ_x (b) shear stress τ_{xz}.

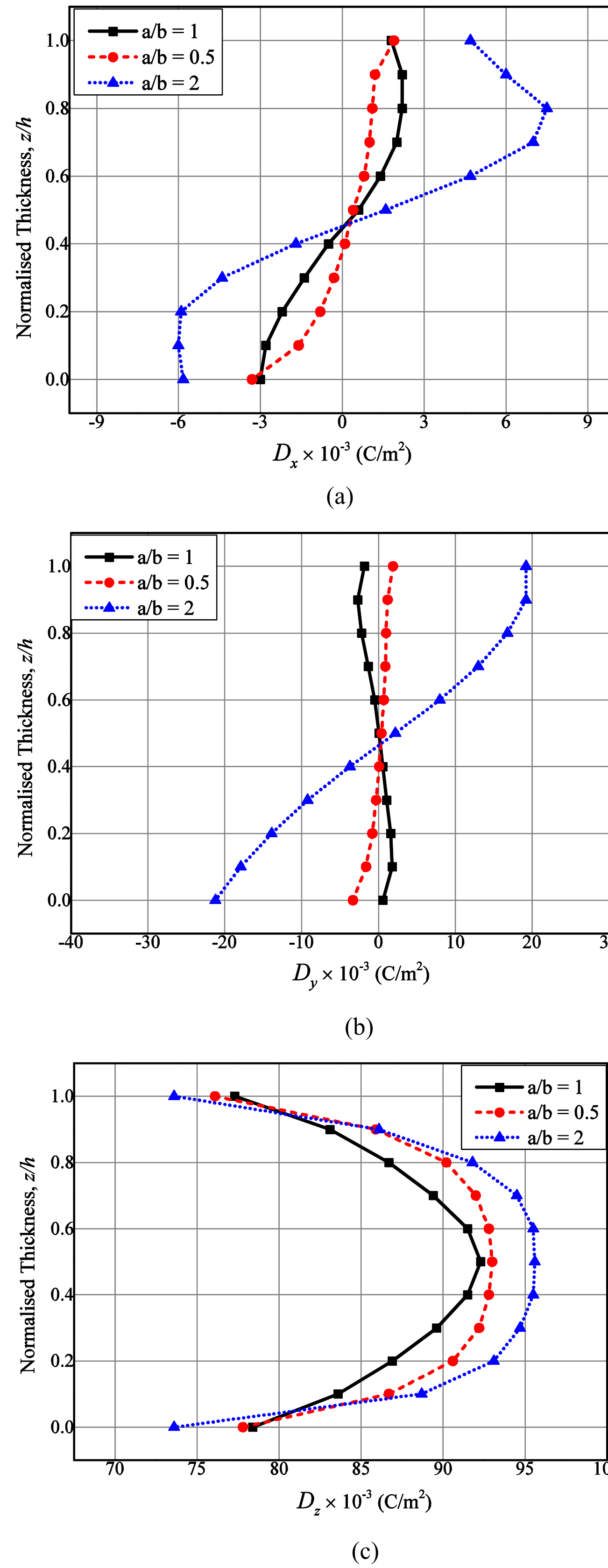

Fig. 20. Effect of length-to-width ratio (a/b) on (a) electric displacement D_x (b) electric displacement D_y (c) electric displacement D_z.

potential of *SFG-BFB* MEE plate with different aspect ratios is evaluated. The results tabulated in Table 14 reveal that the pyroeffects have a predominant benefaction for the *SFG-BFB* MEE plate with higher aspect ratio. Meanwhile, it gradually becomes insignificant for thick MEE plates.

4. Conclusion

This article makes the first attempt to analyse the coupled static response of stepped functionally graded (*SFG*-MEE) plate under different thermal environment. A FE formulation is derived with the aid of the principle of total potential energy and coupled constitutive equations accounting the thermal fields. The variations of direct and derived quantities are evaluated by considering the different temperature distribution. Among the various temperature profiles considered, a significant effect of the uniform temperature distribution is noticed on the static behavior of *SFG*-MEE plate. In addition, a significant effect of *SFG-BFB* stacking sequence is also

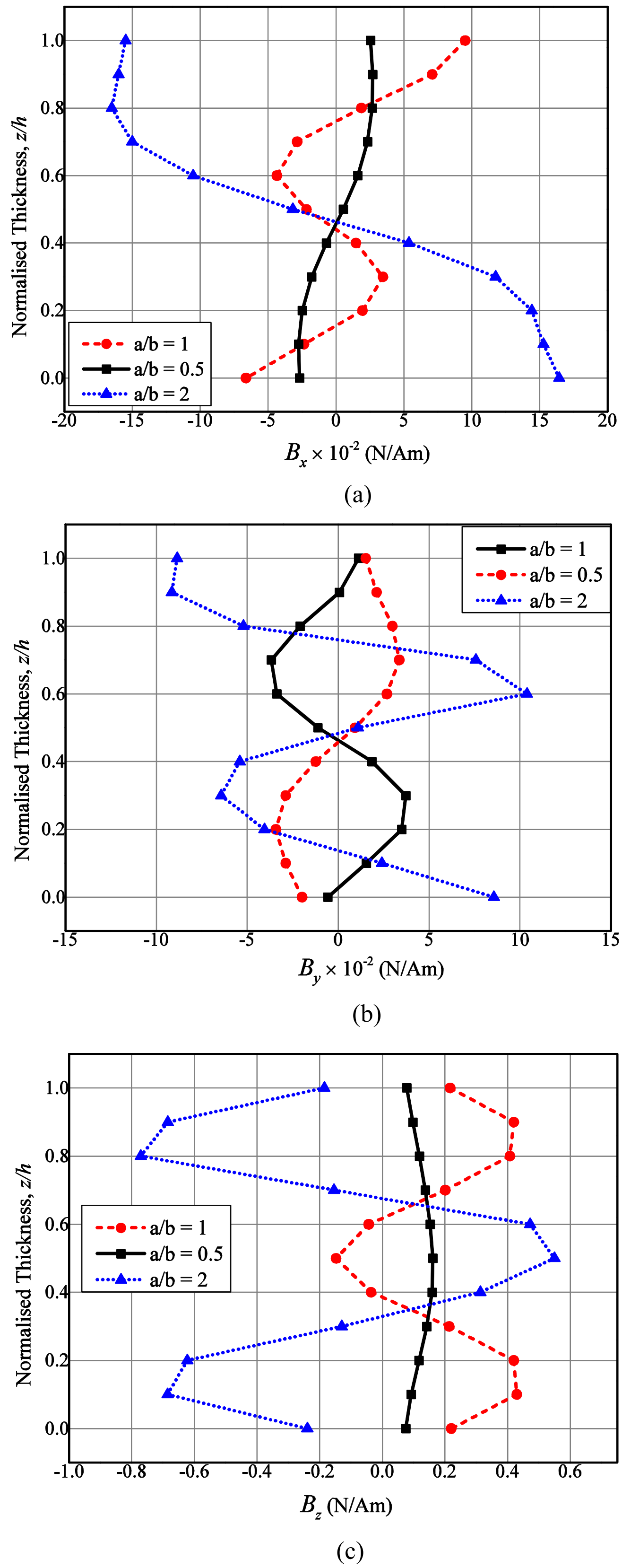

Fig. 21. Effect of length-to-width ratio (a/b) on (a) magnetic flux density B_x (b) magnetic flux density B_y (c) magnetic flux density B_z.

observed on the electric potential and electric displacement components while *SFG-FBF* stacking sequence shows a predominant influence on the magnetic potential and magnetic flux density components. Further, numerical investigation reveals that the lower aspect ratio (a/h) dominates the variation of static parameters across the thickness of the *SFG*-MEE plate. Meanwhile, for

Table 12
Effect of length-to-width (***a/b***) ratio on the maximum values of transverse displacement, electric potential and magnetic potential for different temperature profiles and aspect ratio (***a/h***).

a/h	Temperature profiles	u_z ($\times 10^{-6}$ m)			ϕ (kV)			ψ (A)		
		a/b = 0.5	a/b = 1.0	a/b = 2.0	a/b = 0.5	a/b = 1.0	a/b = 2.0	a/b = 0.5	a/b = 1.0	a/b = 2.0
5	Uniform	7.84	7.76	7.69	16.14	16.28	16.35	24.04	27.48	52.03
	Parabolic	3.31	3.23	3.17	5.79	5.86	5.94	13.44	15.46	37.56
	Linear	5.54	5.46	5.42	9.21	9.28	9.32	19.30	23.67	40.56
	Bi-Triangular	6.83	6.68	6.52	9.56	9.65	9.77	22.52	24.18	43.53
10	Uniform	7.72	7.69	7.51	13.36	13.48	13.53	22.87	27.12	50.06
	Parabolic	3.17	3.14	2.97	5.37	5.41	5.56	11.56	13.73	33.36
	Linear	5.38	5.28	5.19	8.65	8.74	8.82	18.39	21.11	38.39
	Bi-Triangular	6.49	6.38	6.24	9.20	9.23	9.25	20.59	23.87	41.22
50	Uniform	7.67	7.64	7.49	11.21	11.26	11.28	21.15	26.85	49.71
	Parabolic	3.13	3.03	2.91	5.17	5.21	5.30	10.21	12.55	29.42
	Linear	5.21	5.13	5.04	8.59	8.64	8.67	17.35	20.73	35.72
	Bi-Triangular	6.01	5.95	5.83	8.75	8.82	8.93	17.42	20.67	38.13
100	Uniform	7.64	7.55	7.46	11.08	11.13	11.24	19.53	26.76	47.27
	Parabolic	3.07	2.98	2.88	5.10	5.12	5.16	9.87	12.14	28.98
	Linear	5.16	4.97	4.89	8.51	8.54	8.58	16.83	20.08	34.87
	Bi-Triangular	5.98	5.91	5.81	8.63	8.68	8.75	17.11	19.67	35.41

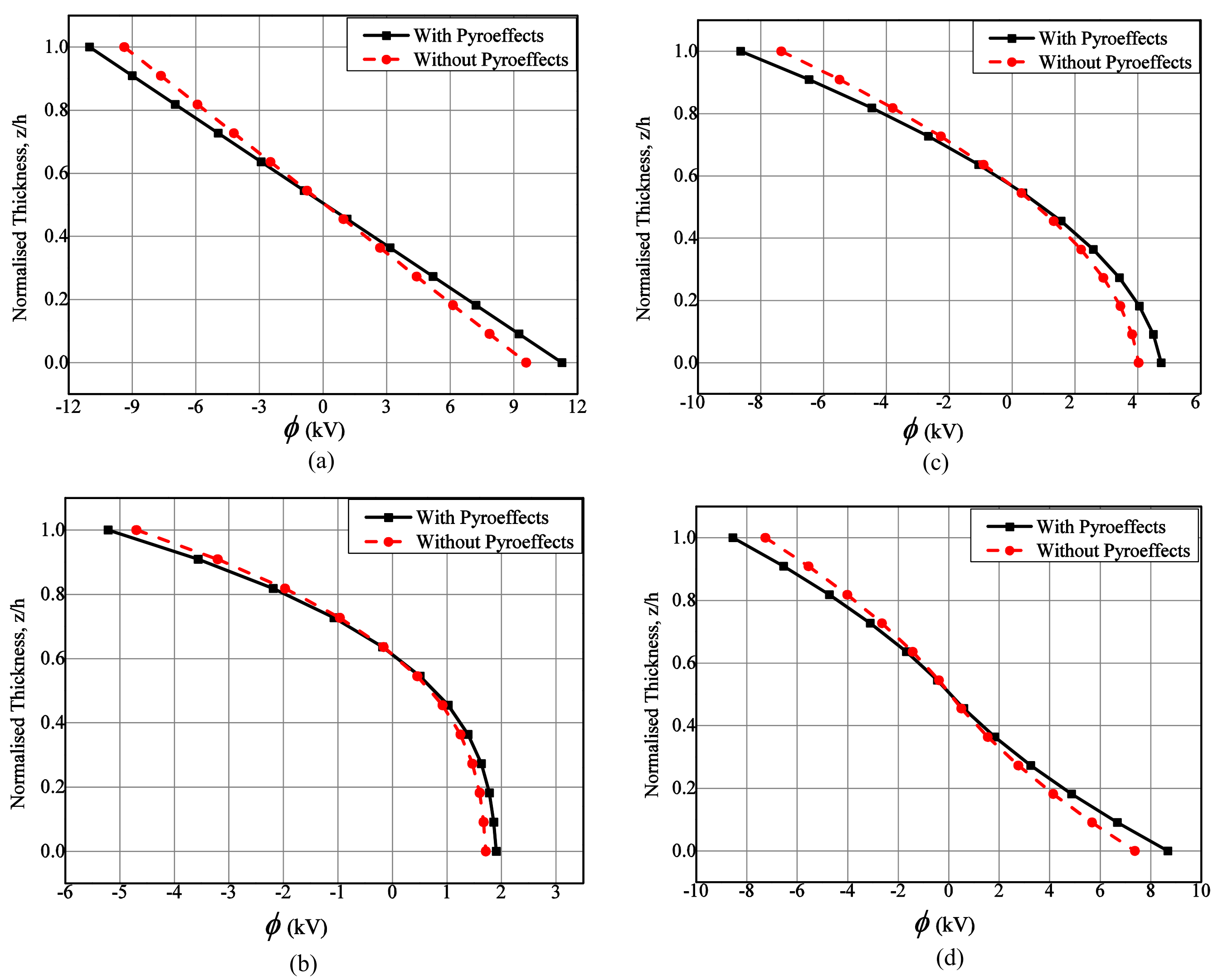

Fig. 22. Pyroeffects on electric potential for (a) uniform (b) parabolic (c) linear (d) bi-triangular temperature distributions.

Table 13
Influence of pyroeffects on the maximum electric potential ϕ_{max} for different stacking sequences.

Temperature Profile	Max. electric potential ϕ_{max} (kV)					
	SFG-BFB			*SFG-FBF*		
	With Pyroeffects	Without Pyroeffects	% Reduction	With Pyroeffects	Without Pyroeffects	% Reduction
Uniform	11.26	9.93	11.82	10.69	9.48	12.62
Parabolic	5.21	4.42	15.16	4.28	3.71	13.3
Linear	8.64	7.65	11.45	7.36	6.48	11.9
Bi-Triangular	8.82	7.24	17.91	7.88	6.74	14.38

Table 14
Effect of aspect ratio (a/h) on the maximum electric potential ϕ_{max} for different temperature profiles.

Temperature profiles	a/h = 100			a/h = 50			a/h = 10			a/h = 5			a/h = 3		
	W.P	Wo. P	% Reduction	W.P	Wo. P	% Reduction	W.P	Wo. P	% Reduction	W.P	Wo. P	% Reduction	W.P	Wo. P	% Reduction
Uniform	9.42	7.06	25.05	11.26	9.93	11.82	11.94	11.48	3.85	12.2	11.9	2.46	13.1	12.88	1.68
Parabolic	4.86	3.64	25.10	5.21	4.42	15.16	5.71	5.44	4.73	6.43	6.18	3.93	7.45	7.26	2.48
Linear	7.23	5.42	25.03	8.64	7.65	11.45	9.06	8.78	3.09	9.61	9.40	2.18	10.18	10.05	1.27
Bi-Triangular	7.38	5.47	25.88	8.82	7.24	17.91	9.42	8.89	5.61	10.06	9.63	4.21	10.87	10.51	3.31

where, W.P – with pyroeffects; Wo. P – without pyroeffects.

the given aspect ratio, decreasing the length-to-width (a/b) ratio results in a higher value of displacement components. However, the electric potential, magnetic potential and the stress components tend to increase with the higher length-to-width (a/b) ratio. The study on the effect of boundary conditions also reveals that the CCCC boundary edge exhibits a significant effect on the transverse displacement, electric potential, normal stress and the electric displacement components. A prominent evaluation is carried out to investigate the influence of pyroeffects. It is observed that irrespective of the temperature profiles, the pyroeffects tends to improve the electric potential of the system. In contrast to the other temperature profiles, the bi-triangular temperature profile exhibits a significant reduction in the electric potential of the system when the pyroeffects are neglected. Moreover, the predominant influence of pyro coupling diminishes as the aspect ratio of *SFG*-MEE plate decreases i.e., for thick *SFG*-MEE plates. It is expected that the results presented here can provide a significant input in the design and analysis of *SFG*-MEE structures under thermal environment.

Appendix A: List of notation

a	Length of the SFG-MEE plate
B_x, B_y, B_z	Electric displacement components along *x,y* and *z* directions
b	Width of the *SFG*-MEE plate
D_x, D_y, D_z	Magnetic flux density components along *x,y* and *z* directions
h	Thickness of the *SFG*-MEE plate
K	Kelvin
L_t, L_ϕ, L_ψ	Differential operators
N	Total number of layers
n	Layer number under consideration
Q^ϕ	Electric charge density
Q^ψ	Magnetic charge density
T_p	Total potential energy of the overall *SFG*-MEE plate
u_x, u_y, u_z	Displacement components along *x*, *y* and *z* directions
V^n	Volume of the n^{th} layer of the *SFG*-MEE plate
V_f	Volume fraction of Barium Titanate ($BaTiO_3$) and Cobalt Ferric oxide ($CoFe_2O_4$)
z	Position of the point of interest from the bottom layer
Matrices and vectors	
$\{B^n\}$	Magnetic flux density vector of the n^{th} layer of the *SFG*-MEE plate
$[B_t], [B_\phi], [B_\psi]$	Derivative of shape function matrices
$[C^n]$	Elastic stiffness matrix of the n^{th} layer of the *SFG*-MEE plate
$\{d_t^e\}$	The nodal displacement vector
$\{D^n\}$	Electric displacement vector of the n^{th} layer of the *SFG*-MEE plate
$[e^n]$	Piezoelectric coefficient matrix of the n^{th} layer of the *SFG*-MEE plate
$\{E^n\}$	Electric field vector of the n^{th} layer of the *SFG*-MEE plate
$\{F_{body}\}$	Body force
$\{F_{conc}\}$	Point force
$\{F_{eq}\}$	Equivalent force vector
$\{F_m^e\}^T$	Elemental mechanical load vector
$\{F_{p.e}^g\}$	Global pyroelectric load vector
$\{F_{p.m}^g\}$	Global pyromagnetic load vector
$\{F_{surface}\}$	Surface force
$\{F_{th}^g\}$	Global thermal load vector
$\{F_\phi^e\}^T$	Elemental electric load vector
$\{F_\psi^e\}^T$	Elemental magnetic load vector
$\{H^n\}$	Magnetic field vector of the n^{th} layer of the *SFG*-MEE plate
$[K_{eq}]$	Equivalent stiffness matrix
$[K_{tt}^g]$	Global elastic stiffness matrix
$[K_{t\phi}^g]$	Global electro-elastic coupling stiffness matrix
$[K_{t\psi}^g]$	Global magneto-elastic coupling stiffness matrix
$[K_{\phi\phi}^g]$	Global electric stiffness matrix
$[K_{\psi\psi}^g]$	Global magnetic stiffness matrix

$[K^g_{\phi\psi}]$	Global electro-magnetic stiffness matrix
$[m^n]$	Electromagnetic coefficient matrix of the n^{th} layer of the *SFG*-MEE plate
$[N_t], [N_\phi], [N_\psi]$	Nodal shape function matrices
$\{p^n\}$	Pyroelectric coefficient vector of the n^{th} layer of the *SFG*-MEE plate
$[q^n]$	Magnetostrictive coefficient matrix of the n^{th} layer of the *SFG*-MEE plate
Greek symbols	
ϕ	Electric potential
ψ	Magnetic potential
$\Delta\theta$	Temperature rise
θ_{max}	The maximum temperature
θ_0	Stress free temperature
θ_i	Initial temperature at the bottom layer of *SFG*-MEE plate
$\{\sigma^n\}$	Stress tensor of the n^{th} layer of the *SFG*-MEE plate
$\{\lambda^n\}$	Thermal stress tensor of the n^{th} layer of the *SFG*-MEE plate
$\{\alpha^n\}$	Thermal expansion co-efficient vector of the n^{th} layer of *SFG*-MEE plate
$\{\varepsilon^n\}$	Strain tensor of the n^{th} layer of the *SFG*-MEE plate
$[\eta^n]$	Dielectric constant matrix of the n^{th} layer of the *SFG*-MEE plate
$\{\tau^n\}$	Pyromagnetic coefficient vector of the n^{th} layer of the *SFG*-MEE plate
$[\mu^n]$	Magnetic permeability constant matrix of the n^{th} layer of the *SFG*-MEE plate
$\{\phi^e\}$	The nodal electric potential vector
$\{\psi^e\}$	The nodal magnetic potential vector

Appendix B

The condensation steps involved in obtaining Eq. (15) can be explained as follows:

Considering the Eq. (12.c) and solving for $\{\psi\}$, we obtain

$$\{\psi\} = [K^g_{\psi\psi}]^{-1}[K^g_{t\psi}]^T\{d_t\} - [K^g_{\psi\psi}]^{-1}[K^g_{\phi\psi}]^T\{\phi\} - [K^g_{\psi\psi}]^{-1}\{F^g_{p.m}\} \tag{B.1}$$

Substituting Eq. (B.1) in Eq. (12.b) and solving for $\{\phi\}$, we get

$$[K^g_{t\phi}]^T\{d_t\} - [K^g_{\phi\phi}]\{\phi\} - [K^g_{\phi\psi}][[K^g_{\psi\psi}]^{-1}[K^g_{t\psi}]^T\{d_t\} - [K^g_{\psi\psi}]^{-1}[K^g_{\phi\psi}]^T\{\phi\} - [K^g_{\psi\psi}]^{-1}\{F^g_{p.m}\}] = \{F^g_{p.e}\}$$

$$\{d_t\}[[K^g_{t\phi}]^T - [K^g_{\phi\psi}][K^g_{\psi\psi}]^{-1}[K^g_{t\psi}]^T] - \{\phi\}[[K^g_{\phi\phi}] - [K^g_{\phi\psi}][K^g_{\psi\psi}]^{-1}[K^g_{\phi\psi}]^T] + [K^g_{\phi\psi}][K^g_{\psi\psi}]^{-1}\{F^g_{p.m}\} = \{F^g_{p.e}\}$$

$$[K_1]\{d_t\} - [K_2]\{\phi\} = \{F^g_{p.e}\} - [K^g_{\phi\psi}][K^g_{\psi\psi}]^{-1}\{F^g_{p.m}\}$$

$$[K_1]\{d_t\} - [K_2]\{\phi\} = \{F_{\phi\_sol}\}$$

$$\{\phi\} = [K_2]^{-1}[K_1]\{d_t\} - [K_2]^{-1}\{F_{\phi\_sol}\} \tag{B.2}$$

Further, on substituting Eqs. (B.1) and (B.2) in Eq. (12.a), we obtain

$$[K^g_{tt}]\{d_t\} + [K^g_{t\phi}]\{\phi\} + [K^g_{t\psi}][[K^g_{\psi\psi}]^{-1}[K^g_{t\psi}]^T\{d_t\} - [K^g_{\psi\psi}]^{-1}[K^g_{\phi\psi}]^T\{\phi\} - [K^g_{\psi\psi}]^{-1}\{F^g_{p.m}\}] = \{F^g_{th}\}$$

$$\{d_t\}[[K^g_{tt}] + [K^g_{t\psi}][K^g_{\psi\psi}]^{-1}[K^g_{t\psi}]^T] + \{\phi\}[[K^g_{t\phi}] - [K^g_{t\psi}][K^g_{\psi\psi}]^{-1}[K^g_{\phi\psi}]^T] - [K^g_{t\psi}][K^g_{\psi\psi}]^{-1}\{F^g_{p.m}\} = \{F^g_{th}\}$$

$$[K_5]\{d_t\} + [K_6]\{\phi\} - [K^g_{t\psi}][K^g_{\psi\psi}]^{-1}\{F^g_{p.m}\} = \{F^g_{th}\}$$

$$[K_5]\{d_t\} + [K_6][[K_3]\{d_t\} - [K_2]^{-1}\{F_{\phi\_sol}\}] - [K^g_{t\psi}][K^g_{\psi\psi}]^{-1}\{F^g_{p.m}\} = \{F^g_{th}\}$$

$$[[K_5] + [K_6][K_3]]\{d_t\} - [K_6][K_2]^{-1}\{F^g_{p.e}\} + [[K_6][K_4] - [[K^g_{t\psi}][K^g_{\psi\psi}]^{-1}]]\{F^g_{p.m}\} = \{F^g_{th}\}$$

$$[K_7]\{d_t\} = [K_6][K_2]^{-1}\{F^g_{p.e}\} + [[K^g_{t\psi}][K^g_{\psi\psi}]^{-1} - [K_6][K_4]]\{F^g_{p.m}\} + \{F^g_{th}\}$$

$$[K_7]\{d_t\} = [K_8]\{F^g_{p.e}\} + [K_9]\{F^g_{p.m}\} + \{F^g_{th}\}$$

$$[K_{eq}]\{d_t\} = \{F_{eq}\} \tag{B.3}$$

The various stiffness matrices and force vectors appearing in Eq. (15) are given by

$$[K_1] = [K^g_{\phi t}] - [K^g_{\psi\phi}][K^g_{\psi\psi}]^{-1}[K^g_{\psi t}], [K_2] = [K^g_{\phi\phi}] - [K^g_{\psi\phi}][K^g_{\psi\psi}]^{-1}[K^g_{\phi\psi}], [K_3] = [K_2]^{-1}[K_1]$$

$$[K_4] = [K_2]^{-1}[K^g_{\psi\phi}][K^g_{\psi\psi}], [K_5] = [K^g_{tt}] + [K^g_{t\psi}][K^g_{\psi\psi}]^{-1}[K^g_{\psi t}][K_6] = [K^g_{t\phi}] - [K^g_{t\psi}][K^g_{\psi\psi}]^{-1}[K^g_{\phi\psi}],$$

$$[K_7] = [K_5] + [K_6][K_3], [K_8] = [K_6][K_2]^{-1}, [K_9] = [K^g_{t\psi}][K^g_{\psi\psi}]^{-1} - [K_6][K_4], [K_{eq}] = [K_7],$$

$$[K_{1\_\psi}] = [K^g_{\psi t}] - [K^g_{\psi\phi}][K_3], [K_{2\_\psi}] = [K^g_{\psi\psi}]^{-1}[K^g_{\psi\phi}][K_2]^{-1},$$

$$[K_{3\_\psi}] = [K^g_{\psi\psi}]^{-1}[K^g_{\psi\phi}][K_2]^{-1}[K^g_{\psi\phi}]^T[K^g_{\psi\psi}]^{-1} + [K^g_{\psi\psi}]^{-1}, \{F_{eq}\} = [K_9]\{F^g_{p.m}\} + [K_8]\{F^g_{p.e}\} + \{F^g_{th}\},$$

$$\{F_{\phi\_sol}\} = \{F^g_{p.e}\} - [K^g_{\psi\phi}]^T[K^g_{\psi\psi}]^{-1}\{F^g_{p.m}\} \tag{B.4}$$

References

[1] Pan E. Exact solution for simply supported and multilayered magneto-electro-elastic plates. J Appl Mech-Trans ASME 2001;68:608–18.
[2] Pan E, Heyliger PR. Free vibrations of simply supported and multilayered magneto-electro-elastic plates. J Sound Vib 2002;252(3):429–42.
[3] Wang Y, Xu R, Ding H, Chen J. Three-dimensional exact solutions for free vibrations of simply supported magneto-electro-elastic cylindrical panels. Int J Eng Sci 2010;48:1778–96.
[4] Ramirez F, Heyliger PR, Pan E. Free vibration response of two-dimensional magneto-electro-elastic laminated plates. J Sound Vib 2006;292:626–44.
[5] Ramirez F, Heyliger PR, Pan E. Discrete layer solution to free vibrations of functionally graded magneto-electro-elastic plates. Mech Adv Mater Struct 2006;13(3):249–66.
[6] Chen WQ, Lee KY, Ding HJ. On free vibration of non-homogeneous transversely isotropic magneto-electro-elastic plates. J Sound Vib 2005;279(1):237–51.
[7] Chen JY, Heyliger PR, Pan E. Free vibration of three-dimensional multilayered magneto-electro-elastic plates under combined clamped/free boundary conditions. J Sound Vib 2014;333(17):4017–29.
[8] Chen J, Chen H, Pan E, Heyliger PR. Modal analysis of magneto-electro-elastic plates using the state-vector approach. J Sound Vib 2007;304:722–34.
[9] Wang J, Qu L, Qian F. State vector approach of free vibration analysis of magneto–electro-elastic hybrid laminated plates. Compos Struct 2010;92(6):1318–24.
[10] Xin L, Hu Z. Free vibration of simply supported and multilayered magneto-electro-elastic plates. Compos Struct 2015;121:344–50.
[11] Wang J, Chen L, Fang S. State vector approach to analysis of multilayered magneto-electro-elastic plates. Int J Solids Struct 2003;40(7):1669–80.
[12] Buchanan GR. Layered versus multiphase magneto-electro-elastic composites. Compos Part B Eng 2004;35(5):413–20.
[13] Annigeri AR, Ganesan N, Swarnamani S. Free vibration behavior of multiphase and layered magneto-electro-elastic beam. J Sound Vib 2007;299:44–63.
[14] Annigeri AR, Ganesan N, Swarnamani S. Free vibrations of simply supported layered and multiphase magneto-electro-elastic cylindrical shells. Smart Mater Struct 2006;15(2):459–67.

[15] Tsai YH, Wu CP. Dynamic responses of functionally graded magneto-electro-elastic shells with open circuit surface conditions. Int J Eng Sci 2008;46:843–57.
[16] Ebrahimi F, Barati MR. A nonlocal higher-order magneto electro visco-elastic beam model for dynamic analysis of smart nanostructures. Int J Eng Sci 2016;107:183–96.
[17] Shooshtari A, Razavi S. Vibration analysis of a magnetoelectroelastic rectangular plate based on a higher-order shear deformation theory. Latin Am J Sol Struct 2016;13:554–72.
[18] Kattimani SC, Ray MC. Smart damping of geometrically nonlinear vibrations of magneto-electro-elastic plates. Compos Struct 2014;14:51–63.
[19] Kattimani SC, Ray MC. Active control of large amplitude vibrations of smart magneto-electro-elastic doubly curved shells. Int J Mech Mater Des 2014;10(4):351–78.
[20] Kattimani SC, Ray MC. Control of geometrically nonlinear vibrations of functionally graded magneto-electro-elastic plates. Int J Mech Sci 2015;99:154–67.
[21] Panda S, Ray MC. Active constrained layer damping of geometrically non-linear vibrations of functionally graded plates using piezoelectric fiber reinforced composites. Smart Mater Struct 2008;17:025012.
[22] Sarangi SK, Ray MC. Smart control of nonlinear vibrations of doubly curved functionally graded laminated composite shells under a thermal environment using 1–3 piezoelectric composites. Int J Mech Mater Des 2013;9:253–80.
[23] Lage RG, Soares CMM, Soares CAM, Reddy JN. Layerwise partial mixed finite element analysis of magneto-electro-elastic plates. Comput Struct 2004;82:1293–301.
[24] Pan E, Han F. Exact solutions for functionally graded and layered magneto-electro-elastic plates. Int J Eng Sci 2005;43:321–39.
[25] Bhangale RK, Ganesan N. Static analysis of simply supported functionally graded and layered magneto-electro-elastic plates. Int J Solids Struct 2006;43(10):3230–53.
[26] Wu CP, Tsai YH. Static behavior of functionally graded magneto-electro-elastic shells under electric displacement and magnetic flux. Int J Eng Sci 2007;45:744–69.
[27] Huang DJ, Ding HJ, Chen WQ. Analytical solution for functionally graded magneto-electro-elastic plane beams. Int J Eng Sci 2007;45:467–85.
[28] Alaimo A, Benedetti I, Milazzo A. A finite element formulation for large deflection of multilayered magneto-electro-elastic plates. Compos Struct 2014;107:643–53.
[29] Zheng Y, Chen T, Wang F, Chen C. Nonlinear responses of Rectangular magnetoelectroelastic plates with transverse shear deformation. Key Eng Mater 2016;689:103–7.
[30] Pan E, Waksmanski N. Deformation of a layered magnetoelectroelastic simply-supported plate with nonlocal effect, an analytical three-dimensional solution. Smart Mater Struct 2016;25:095013.
[31] Sladek J, Sladek V, Chen CS, Young DL. Analysis of circular magnetoelectroelastic plates with functionally graded material properties. Mech Adv Mater Struct 2014;22(6):479–89.
[32] Sladek J, Sladek V, Krahulec S, Pan E. The MLPG analyses of large deflections of magnetoelectroelastic plates. Eng Anal Bound Elem 2013;37(4):673–82.
[33] Sladek J, Sladek V, Krahulec S, Pan E. Analyses of functionally graded plates with a magnetoelectroelastic layer. Smart Mater Struct 2013;22(3):035003.
[34] Wang R, Pan E. Three-dimensional modeling of functionally graded multiferroic composites. Mech Adv Mater Struct 2011;18(1):68–76.
[35] Nazargah ML, Cheraghi N. An exact Peano series solution for bending analysis of imperfect layered functionally graded neutral magneto-electro-elastic plates resting on elastic foundations. Mech Adv Mater Struct 2017;24(3):183–99.
[36] Li YS. Buckling analysis of magnetoelectroelastic plate resting on Pasternak elastic foundation. Mech Res Commun 2014;56:104–14.
[37] Kumaravel A, Ganesan N, Sethuraman R. Buckling and vibration analysis of layered and multiphase magnetoelectroelastic cylinders subjected to uniform thermal loading. Multidiscipline Model Mater Struct 2010;6(4):475–92.
[38] Lang Z, Xuewu L. Buckling and vibration analysis of functionally graded magneto-electro-thermo-elastic circular cylindrical shells. Appl Math Model 2013;37:2279–92.
[39] Ebrahimi F, Barati MR. Static stability analysis of smart magneto-electro-elastic heterogeneous nanoplates embedded in an elastic medium based on a four-variable refined plate theory. Smart Mater Struct 2016;25:105014.
[40] Loja MA, Soares CM, Barbosa JI. Optimization of magneto-electro-elastic composite structures using differential evolution. Compos Struct 2014;107:276–87.
[41] Sun KH, Kim YY. Layout design optimization for magneto-electro-elastic laminate composites for maximized energy conversion under mechanical loading. Smart Mater Struct 2010;19(5):055008.
[42] Kuo HY, Wang YL. Optimization of magnetoelectricity in multiferroic fibrous composites. Mech Mater 2012;50:88–99.
[43] Sunar M, Al-Garni AZ, Ali MH, Kahraman R. Finite element modeling of thermopiezomagnetic smart structures. AIAA J 2002;40:1845–51.
[44] Badri TM, Al-Kayiem HH. Analytical solution for simply supported and multilayered Magneto-Electro-Elastic Plates. Asian J Sci Res 2013;6:236–44.
[45] Ootao Y, Tanigawa Y. Transient analysis of multilayered magneto-electro-thermoelastic strip due to nonuniform heat supply. Compos Struct 2005;68:471–80.
[46] Kumaravel A, Ganesan N, Sethuraman R. Steady-state analysis of a three-layered electro-magneto-elastic strip in a thermal environment. Smart Mater Struct 2007;16(2):282–95.
[47] Kondaiah P, Shankar K, Ganesan N. Pyroelectric and pyromagnetic effects on behavior of magneto-electro-elastic plate. Coupled Syst Mech 2013;2:1–22.
[48] Kondaiah P, Shankar K, Ganesan N. Studies on magneto-electro-elastic cantilever beam under thermal environment. Coupled Syst Mech 2012;1(2):205–17.
[49] Kondaiah P, Shankar K, Ganesan N. Pyroelectric and pyromagnetic effects on multiphase magneto–electro–elastic cylindrical shells for axisymmetric temperature. Smart Mater Struct 2013;22:5007.
[50] Akbarzadeh A, Chen Z. Thermo-magneto-electro-elastic response of rotating hollow cylinders. Mech Adv Mater Struct 2014;21:67–80.
[51] Ebrahimi F, Barati MR. Dynamic modeling of a thermo-piezo-electrically actuated nanosize beam subjected to a magnetic field. Appl Phys A 2016;122:451.
[52] Kim JY, Li Z, Baltazar A. Pyroelectric and pyromagnetic coefficients of functionally graded multilayered multiferroic composites. Acta Mech 2012;223(4):849–60.